Methodical selection of thermal conductivity models for porous silica-based media with variation of gas type and pressure

Sebastian Sonnick [a,b,*], Lars Erlbeck [a], Manuel Meier [b], Hermann Nirschl [b], Matthias Rädle [a]

[a] *Mannheim University of Applied Sciences, Paul-Wittsack-Straße 10, Mannheim, 68163, Germany*
[b] *Karlsruhe Institute of Technology, Straße am Forum 8, Karlsruhe, 76131, Germany*

ABSTRACT

If the effective thermal conductivity of a silica powder in any gas atmosphere is to be calculated analytically, one is faced with a whole series of decisions. There are a lot of different models for the gas thermal conductivity in the pores, the thermal accommodation coefficient or the effective thermal conductivity itself in the literature. Furthermore, it has to be decided which input parameters should be used. This paper gives an overview and recommendations as to which calculation methods are best suited for the material classes of precipitated silica, fumed silica, silica gel and glass spheres. All combinations of the described methods result in a total of 2800 calculation models which are compared with pressure-dependent thermal conductivity measurements of 15 powdery materials with 7 different gases using Matlab computations. The results show that with a model based on a spherical unit cell, which considers local Knudsen numbers, the measuring points of all powder-gas combinations can be determined best with an average variance of about 18.5%. If the material class is known beforehand, the result can be predicted with an average accuracy of about 10% with the correspondingly determined methods.

1. Introduction

The calculation of the effective thermal conductivity of porous media has concerned scientists for more than a century. Understanding the influence of the different heat transfer mechanisms is fundamental in many fields like super insulation materials [1,2], astronomy [3,4], reactor technology, fluidized beds and many more. There is an almost infinite number of numerical [5–7] and analytical [8–10] prediction models. Despite this, or perhaps because of it, the user is often faced with the question of which calculation method is the right one for the own specific case. Tsotsas et al. [11] show an illustrative review of early models of different complexity. Parzinger [12] also provides a very comprehensive listing of 59 different models for the prediction of the effective thermal conductivity of porous media in his thesis. Aichelmayer [13] gives a broad review of different models which he classifies according to their suitability for different solid-fluid conductivity ratios. Bjurström et al. [14] compare several models to calculate the thermal conductivity of silica gel. They obtain the best results with Luikov's model [15] which is also investigated in the present

work. Jayachandran [16] compared measurements of glass-air and ceramic-air packed beds with different models and found good agreement of their 2-D square cylinder unit cell model with measured data. Bouquerel et al. [17] list and compare different models for all heat transfer mechanisms in vacuum insulation panels filled with different silica based core materials. They also show measured values from the literature and make general statements concluding that accurate modeling of gas thermal conductivity is a major challenge.

In the literature empirical fitting parameters are often used to adapt the model results to available measurement results of certain materials [18]. In some cases this approach can make sense, since the investigated porous media can be of very different nature and therefore deviate strongly from the model conceptions. However, in the present work adjustable parameters to give good fits to experimental data will be deliberately avoided in order to demonstrate and compare the raw, unaltered form of the models as they are presented to the end user. Models are often validated with measured values from different authors due to a lack of measurement data. The measurements are often carried out in different laboratories by different people using different methods. In this work, however, all thermal conductivity values originate from the same apparatus and were recorded at the same temperature. Like-

* Corresponding author.
 E-mail address: s.sonnick@hs-mannheim.de (S. Sonnick).

Nomenclature

ETC	Effective thermal conductivity
GTC	Gas thermal conductivity
λ	Thermal conductivity
FS	Fumed silica
PS	Precipitated silica
SG	Silicagel
GS	Glass spheres
d_{peak}	Peak value of pore size measurements
d_{dist}	Pore size distribution
CO_2	Carbon dioxide
SF_6	Sulfur hexafluoride
SO_2	Sulfur dioxide
β	Dimensionless coefficient
Kn	Knudsen number
α	Thermal accommodation coefficient
M_G	Molar mass of gas molecules
M_S	Molar mass of solid surface molecules
T	Temperature
L	Mean free path of gas molecules
k	Boltzmann constant
d_{kin}	Kinetic molecular diameter
p	Pressure
x	Pore size
V	Volume
D_{gr}	Particle size, grain size
d_{pore}	Measured pore size
KC	Kozeny's Correction
ϕ	Porosity
Λ	$1 - \phi$
ϕ_{uc}	Porosity of a unit cell
ϕ_{corr}	Corrected porosity which accounts for λ_g
Nu_r	Empirical parameter for radiation in ZBS model
S	Mean-variance between progressions of measured and calculatet thermal conductivity over pressure curve
N	Number of materials investigated
J	Number of gases investigated
D_{aggl}	Agglomerate size
D_{aggr}	Aggregate size
D_{prim}	Primary particle size

Indices

base	Related to $\lambda_s + \lambda_r$ (measured at very low pressures)
c	Related to the coupling between λ_s and λ_g
eff,SV	Effective, calculated with Schumann and Voss model
g	Gas inside pores
g'	Gas in specific pore size
m	Measured
0	At ambient conditions
p	Particle
r	Radiation
s	Solid backbone of a porous media

wise, the secondary parameters such as pore or particle size distribution were determined using the same and thus comparable methods and were performed with the exact same samples like the thermal conductivity measurements.

In this paper, an overview of a variety of analytical calculation models for the determination of the effective thermal conductivity of porous media is provided. They are classified in terms of their complexity and input parameters. The results of the calculations are compared with thermal conductivity measurements of silica-

based porous materials at different residual gas pressures, using different types of gases (air, helium, argon, CO_2, SO_2, SF_6, and krypton). Six precipitated silicas, three fumed silicas, three silica gels and three glass packed beads were analyzed. Thus, from a chemical point of view, the solid material is the same for all samples studied, although the surface properties may differ. The focus of the investigation is on the heat conduction through the disperse gas phase at varying gas pressures below atmospheric conditions and its coupling with the solid phase. In Chapter 4.1 and 4.2 effective thermal conductivity models which only use the so-called primary parameters are presented. These are the thermal conductivities of the fluid and solid phase as well as the porosity of the materials. The so-called secondary parameters needed for the models in Chapter 4.3 are limited to the particle or pore size or their distributions respectively. Evaluating other models often requires knowledge of additional input parameters like packing arrangement or number of contact points which in general, are not available. Consequently, required data in this work do not go beyond pore- and particle sizes. The mentioned primary and secondary parameters can either be measured directly or taken from the literature. An exception is the gas thermal conductivity inside the pores, since it is a function of the gas pressure and the pore size. In the literature, one can find many options for calculating gaseous thermal conductivity in the pores of porous media with consideration of the Smoluchowski effect. An overview of the most common ones is presented in Chapter 3. The presented effective thermal conductivity (ETC) models are combined with the different gas thermal conductivity (GTC) models and then compared with the measured values. Due to the enormous amount of models and calculation methods in this field, it was impossible to examine all those found in the literature. The aim was to provide an overview of the best-known and most diverse models.

GTC models and ETC models with secondary parameters require pore and/or particle size information. The selection and post-processing of such measurement data represents a decision as difficult and much debated as that of the correct computational model. Therefore, this paper also discusses several options on this issue. Thus, the user ultimately has to reach three basic decisions: which ETC model, which GTC model and which geometric size input parameter should be taken for the particular case. This work will help the user in decision-making, as all the options presented for the three questions are combined and compared with the underlying measurement data using a numerical computing platform. The impacts of the different options are examined and recommendations are made for the four material groups investigated.

2. Materials and methods

2.1. Porous media

In this paper, a total of 15 powdery substances were investigated, all of which consist of amorphous silicone-dioxide (SiO_2). These are six precipitated silicas (PS), three fumed silicas (FS), three silica gels (SG) and three types of glass beads (GS). Five PS samples are from *"W. R. Grace and Company"* (Gr), one is from *"Evonik Industries"* (Ev). The fumed silica samples are from *"Wacker"* (Wa) and *"Evonik Industries"* (Ev). Silica gel samples are all from *"W. R. Grace and Company"* (Gr). Two types of glass spheres are from *"Bassermann Minerals"* (Ba) and the other one is a no-name blasting agent (Bl). Table 1 lists all the solid materials investigated and the specifications available for each. X and ✓ stand for "data unavailable" and "data available", respectively. For materials with a multiscale structure, two or three values are listed for primary particle size D_{prim}, aggregate size D_{aggr} and agglomerate size D_{aggl} in case of fumed or precipitated silica, or D_{prim} and D_{aggl} in case of silica gel. PS and FS have a three-scale struc-

Table 1
List of all investigated porous materials with according available properties. The material names are composed of material type_company_number.

Material	Porosity ϕ [-]	Mean particle size D_{prim} / D_{aggr} / D_{aggl} [μm]	Peak pore size d_{peak} [μm]	Pore size distribution d_{dist}
PS_Gr_01	0.88	0.0208 / 0.1174 / 12.5	0.023	✓
PS_Gr_02	0.91	0.0058 / 0.1738 / 8.9	0.382	✓
PS_Gr_03	0.89	0.0119 / 0.1176 / 8.8	0.008	✓
PS_Gr_04	0.87	0.0198 / 0.1041 / 12.5	0.023	✓
PS_Gr_05	0.81	X / 0.2211 / 7	0.269	✓
PS_Ev[a]	0.88	0.0272 / 0.2119 / 6.5	0.020	✓
FS_Wa	0.94	0.0223 / 0.0944 / 43.1	0.012	✓
FS_Ev	0.93	0.0267 / 0.0564 / 38.9	0.014	✓
FS_VIP[b]	0.90	0.0244 / 0.1390 / 66.9	0.023	✓
SG_Gr_01	0.90	0.0134 / 3.2 / -	0.008	✓
SG_Gr_02	0.90	0.0125 / 11.2 / -	0.008	✓
SG_Gr_03	0.67	0.0038 / 8 / -	1.548	✓
GS_Bl	0.35	56.9 / - / -	17.913	✓
GS_Ba_01	0.56	3.5 / - / -	1.091	✓
GS_Ba_02	0.31	22.2 / - / -	6.273	✓

[a] Hydrophobic PS
[b] Ready mixed core material for vacuum insulation panels, which consists of fumed silica, cellulose fibers and silicon carbide as an opacifier.

Table 2
Material values of the powdery materials used for the calculations.

Thermal conductivity of silica (samples 1 - 12)	1 W/mK	[21]
Density of silica (samples 1 - 12)	2200 kg/m^3	[21]
Thermal conductivity of glass spheres (samples 13 -15)	1.38 W/mK	[22]
Density of glass spheres (samples 13 -15)	2560 kg/m^3	[23]

ture. The primary particles sinter together during the production to form aggregates with sizes in the three-digit nanometer range. These aggregates tend to connect to form the so-called agglomerates due to Van der Waals forces. In the case of silica gels, a large network of primary particles was crushed to form the particles. Here, no further agglomeration is assumed. Therefore, only two size scales are given in the table, the primary particles and the aggregates. Primary particle sizes were measured with a Xenocs Xeuss 2.0 SAXS (small-angle x-ray scattering) camera for all multiscale samples. Agglomerate sizes have been measured by laser diffraction (*Co. Malvern and Co. Sympatec*) using a wet dispersion process. Aggregate sizes have been measured by dynamic light scattering in deionized water using a Zetasizer (*Co. Malvern Panalytical Ltd, UK*) with a 10-minute upstream dispersion step with an ultrasonic tip. The glass sphere sizes were determined by a digital light microscope (*Co. Keyence*). For the pore size distributions mercury intrusion porosimetry measurements using an AutoPore III (*Co. micromeritics, USA*) and a Pascal Series Mercury Intrusion Porosimeter (*Co. Thermo Fisher*) have been carried out. Pore size distributions of all materials are shown in the appendix in Fig. A.1. Some of the presented data have already been published in Meier et al. [19,20]. All solid material values for the different samples are shown in Table 2.

2.2. Gases

The gas pressure-dependent thermal conductivity has been measured for all materials listed in Table 1. For this purpose, all of the gases listed in Table 3 have been used for an individual measurement (except for krypton which was only used for some of the materials due to supply difficulties).

2.3. Thermal conductivity measurements

The gas pressure-dependent thermal conductivity was measured with a self-constructed guarded hot plate apparatus. It is located in a vacuum chamber so that the residual gas atmosphere can be adjusted between approximately 0.05 *mbar* and atmospheric pressure. The special feature of the apparatus is that the entire measuring chamber as well as the hot plate can be removed from the apparatus in order to carry out sample preparation, i.e. compaction of the powdery materials with a hydraulic press directly on site. This avoids cracks and gaps between the plates and the samples as far as possible. A more precise description of the setup and an error consideration can be taken from our earlier work [24]. For sample preparation, the powdered materials are baked and dried directly in the apparatus for at least 3 hours at 95 °C and < 1 *mbar*. The vacuum chamber is purged twice with the regarding gas. Finally, $N = 13$ thermal conductivity values are recorded at gas pressures between 0.05 *mbar* and atmospheric pressure starting at atmospheric pressure.

3. Calculation of the gas thermal conductivity

When calculating the gas thermal conductivity, the dilution of the gas or the type of gas flow is decisive. A measure for this is the Knudsen number (Kn). It is explained in more detail in Chapter 3.2. Kn is often used to categorize into different flow regions. A common classification into molecular flow ($Kn > 10$), transition region ($10 > Kn > 0.1$), slip flow ($0.1 > Kn > 0.01$) and continuum flow ($0.01 > Kn$) was proposed by Chambre [25]. In the continuum region and free molecular flow, the thermal conductivity can easily be derived using the kinetic theory of gases [26]. In the continuum region, the thermal conductivity is almost independent of the pressure because of two mutual canceling effects. For one thing, the more particles are available to transport energy, the higher the thermal conductivity is. Secondly, if there are many particles, the mean free path becomes smaller, thus the energy is not transported as far between the individual collisions, which leads to a reduction of the thermal conductivity. Both effects almost cancel each other out [27]. With increasing Knudsen number, however, the mean free path is increasingly influenced by the particle-wall collisions, and thus by the pore size, rather than by the particle-particle collisions. This behavior results in a pressure dependence and is called Soluchowski or Knudsen effect. An exact derivation of the thermal conductivity of gases in the transition region would be very difficult due to the complexity of the Boltzmann equation. Therefore, it is common to interpolate between the continuum solution and the free molecular flow solution. This results in an equation developed by Prasolov [28] (Eq. 1).

$$\lambda_{gas} = \frac{\lambda_0}{1 + \beta Kn} \tag{1}$$

Table 3

List of gases used for the thermal conductivity measurements and their properties of interest.

	Thermal conductivity $\lambda_0[\frac{W}{mK}]$	Molar mass $M[\frac{g}{mol}]$	Kinetic molecular diameter $d_{kin}[10^{-10}m]$	Isentropic Exponent $(\kappa(\frac{c_p}{c_v})[-])$
Air	0.0262	28.96	3.69	1.4
Helium	0.1536	4.00	2.19	1.68
Argon	0.0177	39.95	3.64	1.68
CO_2	0.0171	44.01	4.55	1.29
Krypton	0.0095	83.8	4.13	1.68
SF_6	0.0135	146.05	6.17	1.29
SO_2	0.0095	64.07	5.42	1.29
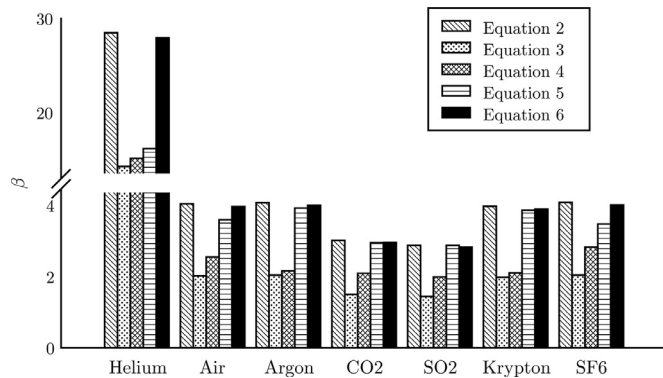
Fig. 1. Dimensionless parameter β for all gas types investigated in this paper calculated with equations from Table 4.

Table 4

Different equations from the literature to calculate the dimensionless parameter β.

Equation	References
$\beta = 2 * \dfrac{2-\alpha}{\alpha}\dfrac{2\kappa}{\kappa+1}\dfrac{1}{Pr}$ (2)	[15,29,30]
$\beta = \dfrac{2-\alpha}{\alpha}\dfrac{2\kappa}{\kappa+1}\dfrac{1}{Pr}$ (3)	[31]
$\beta = 2\dfrac{2-\alpha}{\alpha}$ (4)	[32–34]
$\beta = \dfrac{1}{\alpha}\dfrac{9\kappa-5}{\kappa+1}$ (5)	[35]
$\beta = \dfrac{5\pi}{16}\dfrac{9\kappa-5}{\kappa+1}\dfrac{2-\alpha}{\alpha}$ (6)	[24,36,37]

From the structure of this equation it is clear that $\lim_{Kn\to\infty}\lambda_g(Kn)=0$ and $\lim_{Kn\to0}\lambda_g(Kn)=\lambda_0$. It is well known that gas molecules do not tend to perform a complete energy exchange with the wall during the collision. This leads to a temperature jump at the interface. Mathematically, this phenomenon can also be understood as an increase of the wall distance. In Eq. (1) this effect is represented by the dimensionless parameter β. There are several definitions for β in the literature, which are listed in Table 4. It is a function of at least one of the following parameters: isentropic exponent κ (which is the relation between specific heat at constant pressure and specific heat at constant volume $\frac{c_p}{c_v}$), the thermal accommodation coefficient α (which will be discussed in Chapter 3.1 in detail) and the Prandtl Number Pr. The resulting β values for the investigated gases in combination with a silica surface differ greatly from the gases and also from the equations as can be seen in Fig. 1.

3.1. Accommodation coefficient

The thermal accommodation coefficient (TAC) α is a measure for the imperfection of the energy exchange of a gas molecule at wall impact. The TAC is for heat transport via molecular collisions like the emission coefficient for radiative transfer. Essentially, it depends on the following influencing variables: Molar mass of
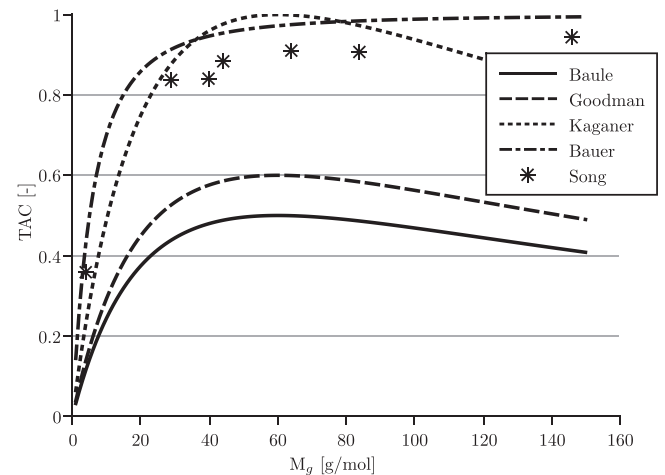
Fig. 2. Accommodation coefficients calculated with different models plotted over the molar mass of the gas molecule. Song's model also depends on degree of freedom of the respective molecule so it was only calculated for the types of gas investigated in this paper.

gas molecules M_G, degrees of freedom of gas molecules, molar mass of the solid surface material M_S, surface properties (roughness, adsorbed molecules, impurities) and temperature. In the literature only a few data are available with partly significant deviations. General agreement exists, however, on the tendency that the accommodation coefficient decreases with increasing temperature and decreasing molar mass of the gas. Some well-known formulas for calculating the accommodation coefficient are given below.

The resulting TACs are plotted against the molar mass of the gas particles in Fig. 2. From the solid sphere theory and the law of conservation of momentum, an approximation of the TAC can be derived from the masses of the gas molecules and the molecules of the solid surface. According to Baule [38], if only translational energy is transferred and each gas particle hits the surface only once, Eq. (7) can be derived.

$$\alpha = \frac{2M_G M_S}{(M_G+M_S)^2} \quad (7)$$

This equation was extended by Goodman [39], who used it to obtain good agreement with measured values in the temperature range 0 - 500 K. He postulated Eq. (8).

$$\alpha = 2.4\frac{\frac{M_G}{M_S}}{\left(1+\frac{M_G}{M_S}\right)^2} \quad (8)$$

Another approximation mentioned by Kaganer [29] is shown in Eq. (9).

$$\alpha = 1-\left(\frac{M_S-M_G}{M_S+M_G}\right)^2 \quad (9)$$

Song [40] not only takes the masses of the molecules but also the degrees of freedome of the gas molecules into account. He de-

rives Eq. (10),

$$\alpha = exp\left[C_0\left(\frac{T-T_0}{T_0}\right)\right]\left(\frac{M_G^*}{C_1+M_G^*}\right)$$
$$+ \left\{1 - exp\left[C_0\left(\frac{T-T_0}{T_0}\right)\right]\right\}\frac{2.4\frac{M_G}{M_S}}{(1+\frac{M_G}{M_S})^2} \tag{10}$$

where $M_G^* = M_G$ for monatomic gases and $M_G^* = 1.4 * M_G$ for diatomic or polyatomic gases and

$C_0 =$	-0.57	dimensionless
$C_1 =$	6.8	units of M_G
$T_0 =$	273	K.

Bauer, on the other hand, describes a negligible influence of the surface properties and recommends for estimation a correlation of the molar mass of the gas and the TAC at room temperature, which is shown only graphically in his paper [41]. The relationship is best described by a function of the form $y = \frac{a}{(x+x_0)^2}$. For this particular case, Eq. (11) could be derived from the figure.

$$\alpha = 1 - \frac{144.6}{(M_G + 12)^2} \tag{11}$$

3.2. The knudsen number and the characteristic length

The Knudsen number is a measure of the dilution of the gas and describes the ratio between the mean free path of the gas molecules L to a characteristic length x ($Kn = L/x$). The higher the Knudsen number, the greater is the dilution of the gas. The mean free path of the gas molecules is the average distance a gas molecule can travel before it collides with another one. It can be calculated according to the kinetic theory of gases via Eq. (12) [42].

$$L = \frac{k\,T}{\sqrt{2}\,\pi\,d_{kin}^2\,p} \tag{12}$$

There are various interpretations in the literature for the characteristic length in a porous material. The original definition by Kaganer [29] refers to two opposing parallel plates. In this case, the distance between the plates is the characteristic length. The situation is different in the void spaces of a porous material. The pore shapes are usually very chaotic and deviate strongly from two opposite plates. Therefore, the aim of an analytical solution is to find the best approximation to reality for different porous media. There are different approaches to this purpose, which will be discussed in the following. Many authors simply use the mean pore size as characteristic length. This assumption deviates relatively strongly from the real conditions, but represents a simple and fast estimation method. Another common method is to use a correction factor for the pore size or, if no pore size measurement data are available, to calculate the pore size from the particle size. Details on this are elucidated in Chapter 3.3. If available, it is possible to use the pore size distribution d_{dist} instead of the mean or peak pore size d_{peak} for the calculation. In this case, a corresponding Knudsen number must be calculated for each occurring pore size, and from this a gas thermal conductivity. It can then be weighted according to the volume fraction associated with the different pore sizes, as it is shown in Eq. (13).

$$\lambda_g = \int \lambda_g' \frac{dV}{V_{max}} dx \tag{13}$$

With λ_g' as gas thermal conductivity in pores with pore size x, dV as pore volume of the pores with size dx and V_{max} as total pore volume.

Table 5
Summary of different methods to calculate gas thermal conductivity in pores.

Dimensionless parameter β	TAC α	Characteristic length x
Eq. (2)	Baule (Eq. 7)	d_{peak}
Eq. (3)	Goodman (Eq. 8)	d_{dist}
Eq. (4)	Kaganer (Eq. 9)	$d_{peak} * \frac{\pi}{6}$
Eq. (5)	Song (Eq. 10)	$d_{dist} * \frac{\pi}{6}$
Eq. (6)	Bauer (Eq. 11)	D_{aggl} & KC
		D_{aggr} & KC
		D_{prim} & KC

3.3. Corrections of the geometric parameters

In addition to the mentioned calculation methods, some suggestions for the correction of the measured quantities exist in order to either convert them into the required parameters or to adapt them to the models. If, for example, no direct measured values for the pore size are available, the Kozeny's correction (KC) for calculating the average gap distance x for equal-sized spherical particles from the particle sizes D_{prim}, D_{aggr} or D_{aggl} and the porosity ϕ can be used [29,43,44]. It results from the ratio of pore volume and particle surface area and is shown in Eq. (14).

$$x = \frac{2}{3}\frac{\phi}{1-\phi}D_{gr} \tag{14}$$

Even if measured values for the pore size or the pore size distribution are available, correction methods can be useful due to the fact that measured pore sizes do not necessarily represent the average gap distance in pores. In our previous works [24,45], the average gap distance in spherical pores was calculated from the pore size with Eq. (15).

$$x = \frac{\pi}{6}d_{pore} \tag{15}$$

3.4. Summary of possible calculation methods for the gas thermal conductivity

The calculation options for the TAC α, the dimensionless parameter β and the characteristic length x described in the previous chapters are summarized in Table 5. The variations result in 175 possible combinations to calculate the gas thermal conductivity with Eq. (1).

4. Calculation of the effective thermal conductivity

The effective thermal conductivity λ_{eff} is the macroscopically observed, apparent thermal conductivity of a material composite or a porous medium. It is composed of the thermal conductivities of the individual components, their proportion and the structural distribution. In the following, various models for predicting the effective thermal conductivity of porous media are presented. Basically, it is assumed that the total thermal conductivity is composed of the four components: solid thermal conductivity λ_s, thermal conductivity by radiation λ_r, gas thermal conductivity λ_g and the coupling term λ_c as it is shown in Eq. (16). Convection can be neglected since the gases are not moving in such small pores [46,47].

$$\lambda_{eff} = \lambda_s + \lambda_r + \lambda_g + \lambda_c \tag{16}$$

The two components λ_s and λ_r are assumed to be independent of gas pressure. Their sum can be determined by thermal conductivity measurements at very low pressures, since it can then be assumed that the thermal conductivity of the gas is completely suppressed. These two mechanisms are represented by the baseline on the bottom of Fig. 3 and are summarized below as λ_{base}. The
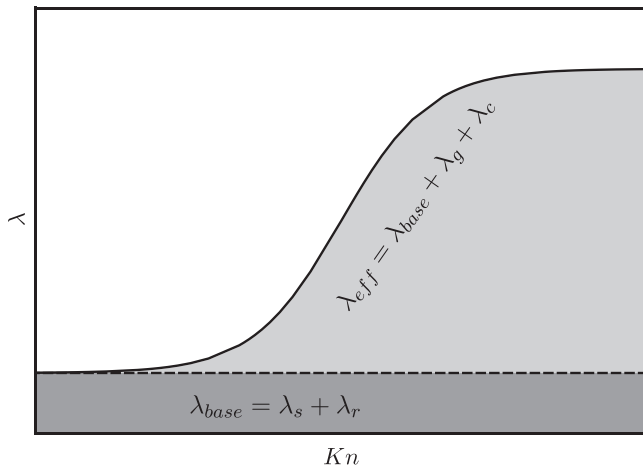
Fig. 3. Schematic diagram of typical thermal conductivity versus Knudsen number curve; x-axis is logarithmic and inverted.

gas thermal conductivity is a function of the Knudsen number Kn, which in turn is a function of pressure as well as of the geometric size of the void space. It can be determined as described in Chapter 3. The coupling term λ_c can be understood as the interaction between the other heat transfer mechanisms, primarily between λ_s and λ_g. For example, having a unit cell of two ideal spheres in contact with infinitesimally small contact area, the solid heat conduction in the direction of the line connecting the two centers of the spheres is also infinitesimally small if the gas heat conduction is completely suppressed. If the gas between the spheres now obtains a non-zero thermal conductivity, the effective thermal conductivity of the entire unit cell exceeds the pure gas thermal conductivity (provided that λ_p is greater than λ_g). Fig. 3 shows not an actual measurement or calculation. It is only a schematic representation to visualize different heat transfer mechanisms.

Different types of prediction models for the effective thermal conductivity of porous media are presented below. According to their approach and complexity, they are divided into the categories "Geometry independent models", "Unit Cell Models" and "Models with consideration of local Knudsen numbers".

4.1. Geometry independent models

For this type of prediction model, one needs minimal knowledge about the investigated materials. It is sufficient to know the thermal conductivities of the two phases and the porosity. These data are called primary parameters in some references. According to [13], these models work best for small solid/fluid thermal conductivity ratios. Accordingly, they should be applicable in the present investigation especially for pressure ranges close to atmospheric pressure and gases with rather high thermal conductivity.

4.1.1. Series and parallel connection model

The simplest model for describing the thermal conductivity of porous media is a serial or parallel connection of the thermal resistances of the individual phases. The weighting of the individual phases is usually done according to their porosity. The pure serial or parallel connection represents the lower and upper limit case. Combinations of the two limiting cases are usually used. The serial part can be understood as the contribution of the coupling effect. A well-known model of this kind was already developed by Russel [48] in 1935. He presented two versions of his formula which differ in which of the two phases is disperse. In the case of powdery substances, the fluid can always be regarded as the disperse phase. The corresponding version is shown in Eq. (17). Since Rus-

sel's model does not provide for a continuous solid path, the effective thermal conductivity approaches zero when the gas thermal conductivity disappears. In order to prevent this and to make the model comparable with the others, the measured value λ_{base} is added to the original equation.

$$\lambda_{eff} = \lambda_{base} + \lambda_g \left(\frac{\Lambda^{2/3} + \frac{\lambda_g}{\lambda_p}\left(1 - \Lambda^{2/3}\right)}{\Lambda^{2/3} - \Lambda + \frac{\lambda_g}{\lambda_p}\left(1 - \Lambda^{2/3} + \Lambda\right)} \right) \quad (17)$$

Λ is $1 - \phi$ and ϕ is the porosity, which is defined as the volumetric ratio of void spaces in a porous media.

4.1.2. Maxwell

Maxwell formulated two limiting cases for very large and very small porosities in his composite medium problem as early as 1873 [49]. The first case mentioned assumes a fluid with suspended sherical solid particles and the second a solid with widely spaced sherical fluid-filled voids. In both cases, the spheres show no interactions with each other. Therefore, λ_{base} is added to the result again. In the present work only the first version is used which is shown in Eq. (18).

$$\lambda_{eff} = \lambda_{base} + \lambda_g \left(\frac{2\phi + \frac{\lambda_p}{\lambda_g}(3 - 2\phi)}{3 - \phi + \frac{\lambda_p}{\lambda_g}\phi} \right) \quad (18)$$

4.1.3. Scaling model

Swimm et al. [36] propose a scaling model that is developed on the basis of simple interconnections of thermal resistances. It provides for a linear dependence of the coupling effect on the gas thermal conductivity for a wide range of solid to fluid thermal conductivity ratios. The corresponding function is shown in Eq. (19).

$$\lambda_{eff} = \lambda_{base} + \lambda_g(1 + F\phi) \quad (19)$$

According to this, in one of our previous works [24], the relationship shown in Eq. (20) was determined for precipitated silica with air as the pore gas and a porosity range between 0.76 and 0.92. For this purpose, the results were fitted to thermal conductivity measurements with F as the only fit parameter. Five different precipitated silicas were used, each of which was compressed to different degrees in order to include as large a porosity range as possible.

$$\lambda_{eff} = \lambda_{base} + \lambda_g(-18.68\phi + 18.94) \quad (20)$$

4.2. Unit cell models

The models discussed in this chapter, consider particle geometry in some way. These are all unit cell models. A unit cell is a substitute geometry for the smallest structures that repeat over and over again in a porous medium. The unit cell geometry is derived from the porosity and/or the particle size.

4.2.1. Sphere model

Kaganer proposes a model for spherical backed beds based on a cylindrical unit cell with two spheres in contact in his 1969 paper [29]. A sketch of this unit cell is shown in Fig. 4. The heat flux at each distance to the contact point is calculated as a series connection from the thermal resistances $\frac{2x'_p}{\lambda_p}$ and $\frac{x'_g}{\lambda_g}$, and weighted as a parallel connection according to their circular area fractions perpendicular to the heat flux direction. The resulting thermal conductivity is then assigned to a certain area fraction of the total heat transfer area via porosity. In addition, the average number of contact points of the spheres is also calculated from the porosity. The effective thermal conductivity after integration over the radius of the cylindrical unit cell finally results in Eq. (21). Again, λ_{base} is added, since the contact points of the spheres are infinitesimally
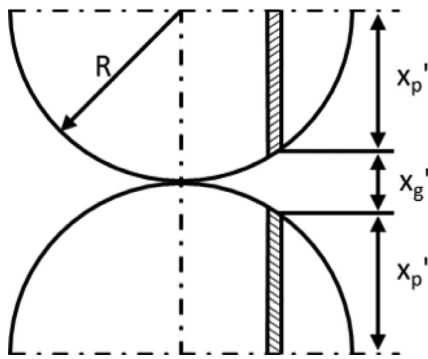
Fig. 4. Cylindrical unit cell of the sphere model.

small and thus the effective thermal conductivity together with the gas thermal conductivity would otherwise approximate zero.

$$\lambda_{eff} = \lambda_{base} + \lambda_g \left[\frac{5.8(1-\phi)^2}{k} \left(\frac{1}{k} \ln \frac{\lambda_p}{\lambda_g} - 1 - \frac{k}{2} \right) + 1 \right] \qquad (21)$$

Here $k = 1 - \frac{\lambda_g}{\lambda_p}$.

Cunnington and Brodt [50,51] also use Eq. (21). In this model, the gas thermal conductivity is independent of the location and is either assumed as $\lambda_g = \lambda_0$ for the case of continuum flow or determined by taking into account the Soulochowski effect via a relationship listed in Chapter 3. Particle size is not considered in this type of computational model. Numerous authors [52,53] present similar unit cell models. They are the attempt to take into account the coupling effect between solid and gas thermal conductivity by the simplified consideration of a geometry as close to reality as possible. It is common to weight the coupling contribution and the pure gas thermal conductivity with corrected porosities for example by comparing the porosity of the unit cell with the real porosity. Some different approaches to this are listed in [54].

4.2.2. Schumann and Voss

The model of Schumann and Voss [55] is based on a planar unit cell with a particle geometry in the form of a hyperbola. The exact function of the hyperbola is determined by a shape factor which is denoted as P in the following. P is related to the porosity of the unit cell ϕ_{uc} as described in Eq. (22).

$$\phi_{uc} = P(P+1) \ln \left(\frac{1+P}{P} \right) - P \qquad (22)$$

Since this equation has a limit value of 0.5, the maximum possible unit cell porosity in this model is $\phi_{uc} = 0.5$. Most of the materials investigated here have a higher porosity than this. For this cases P was assumed to be 200 which leads to a unit cell porosity very close to $\phi_{uc} = 0.5$. Consequently, a corrected porosity ϕ_{corr} is introduced in Eq 23. For the particular case of $\phi_{uc} = 0.5$ the term $\frac{\phi_{uc}}{1-\phi_{uc}}$ becomes one and the corrected porosity can be written as $\phi_{corr} = \phi - (1-\phi)$. For $\phi < 0.5$, $\phi_{corr} = 0$.

$$\phi_{corr} = \phi - (1-\phi) \frac{\phi_{uc}}{1-\phi_{uc}} \qquad (23)$$

The original Schumann and Voss equation for the effective thermal conductivity is shown in Eq. (24).

$$\lambda_{eff,SV}$$
$$= \lambda_g \left(\phi^3 + \frac{\frac{\lambda_s}{\lambda_g}(1-\phi^3)}{1+P\left(1-\frac{\lambda_s}{\lambda_g}\right)} \left[1 + \frac{P(1+P)\left(1-\frac{\lambda_s}{\lambda_g}\right)}{1+P\left(1-\frac{\lambda_s}{\lambda_g}\right)} \ln \left(\frac{1+P}{P\frac{\lambda_s}{\lambda_g}} \right) \right] \right) \qquad (24)$$
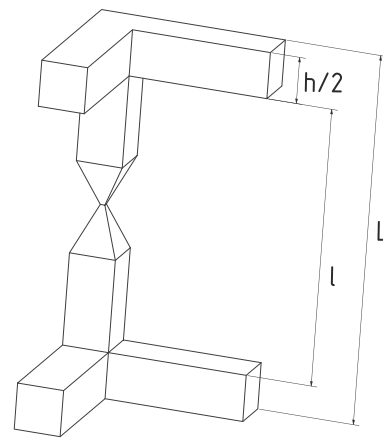
Fig. 5. Unit cell of Luikovs model reconstructed after [15].

To include the corrected porosity and once again to account for λ_{base} at very low pressure levels, the formula was extended as can be seen in Eq. (25).

$$\lambda_{eff} = \lambda_{base} + (1-\phi_{corr}) * \lambda_{eff,SV} + \phi_{corr} * \lambda_g \qquad (25)$$

4.2.3. Luikov

The unit cell presented by Luikov et al. [15] consists of a skeleton of thermal resistors, as can be seen in Fig. 5. The spot in the middle accounts for the contact resistance between particles. The geometric sizes of the unit cell L and l can be calculated from the particle size and the porosity of the bulk material.

In the original literature the relation $\frac{h}{l}$ is given in tabular form only. In the present work the polynomic equation shown in Eq. (26) with a coefficient of determination of 0.9995 was used instead.

$$\frac{h}{l} = 209.03\phi^6 - 744.65\phi^5 + 1054.40\phi^4 - 762.77\phi^3$$
$$+ 304.07\phi^2 - 68.73\phi + 8.70 \qquad (26)$$

Luikov's method for the calculation of the effective thermal conductivity is shown in Eq. (27).

$$\lambda_{eff} = \frac{1}{\frac{1}{\left(\frac{h}{L}\right)^2} + A} + v_g * \left(1 - \frac{h}{L} \right)^2 + \frac{2}{1 + \frac{h}{L} + \frac{1}{v_g \frac{h}{L}}} \qquad (27)$$

Where

$$A = \frac{1}{\frac{\lambda_c}{\lambda_p} + \frac{v_g}{4k_k k_m} \left(\frac{h}{L} \right)^2 * 10^3}$$

$$\frac{h}{L} = \frac{\frac{h}{l}}{1 + \frac{h}{l}}$$

and

$$v_g = \frac{\lambda_g}{\lambda_p}$$

The factors k_m and k_k are an empirical coefficient and the coefficient of particle adhesion, respectively. They are assumed to be $k_m = 1$ and $k_k = 1.5$ according to an example calculation in the original paper. For λ_c the following term is used to ensure that the thermal conductivity at very low pressures corresponds to the measured one. This is again due to comparability to the other models.

$$\lambda_c = \frac{\lambda_p}{\frac{\lambda_p}{\lambda_{base}} - \frac{1}{\left(\frac{h}{L}\right)^2}}$$

4.2.4. Zehner, Bauer, Schlünder

In their 1970 paper [56], Zehner, Bauer, and Schlünder developed what is probably the best-known model for bulk particles of different geometries. They introduced the shape factor C which determines the geometry of the model particle in a unit cell. The formula for determining the particle geometry is shown in Eq. (28).

$$r^2 + \frac{z^2}{(B - (B-1)x)^2} = 1 \tag{28}$$

Where

$$B = C\left(\frac{1-\phi}{\phi}\right)^{\frac{10}{9}}$$

For spherical fillings, $C = 1.25$ as suggested by the authors. Since no recommendation was made for multi-scale geometries and hierarchical structures, $C = 1.25$ is used in this work for all materials. The resulting model particle geometry, however, does not correspond to a sphere. This is explained by the fact that one tries to compensate errors which are made by the assumption of parallel heat flow lines in the following procedure. The final function for the effective thermal conductivity, obtained by integration over the radius of the unit cell is given in Eq. (29).

$$\lambda_{eff} = \lambda_{base} + \lambda_g * \left\{ \left(1 - \sqrt{1-\phi}\right) + \sqrt{1-\phi}\frac{2}{1-\frac{\lambda_g}{\lambda_p}B} \right.$$
$$\left[\frac{\left(1-\frac{\lambda_g}{\lambda_p}\right)B}{\left(1-\frac{\lambda_g}{\lambda_p}B\right)^2} \ln\frac{\lambda_p}{B\lambda_g} - \frac{B+1}{2} - \frac{B-1}{1-\frac{\lambda_g}{\lambda_p}B} \right] \right\} \tag{29}$$

In Eq. (29) the pure gas thermal conductivity is weighted with the corrected porosity $\left(1 - \sqrt{1-\phi}\right)$ and the coupling part determined with the unit cell with $\sqrt{1-\phi}$ respectively. This relationship was derived using the analogy of heat conduction and diffusion and was determined by measuring diffusion coefficients of porous media.

The Zehner, Bauer, Schlünder model is often called ZBS-model and is used and sometimes modified by many researchers. Sih and Barlow [57] for example postulated a modified form and compared it with 424 measured data. The comparison shows the predictions to be accurate within a range of ± 30% relative error.

4.3. Unit cell models with consideration of local Knudsen numbers

In the models shown in 4.1 and 4.2, a homogeneous thermal conductivity over the entire gas space is assumed. However, this leads to an inaccurate representation of reality in the Knudsen range, since the thermal conductivity depends on the distance to the wall at each point. If one assumes locally different Knudsen numbers in the void space, correspondingly varying gas thermal conductivities result over the radius of the unit cell. Near the contact point of the particles, small gap widths x'_g (Fig. 4) with high Knudsen numbers occur. As one moves further away from the point of contact in the x-direction, the gap width increases and Kn decreases. This results in a variation of the total thermal conductivity of the unit cell that depends on the particle size. As in the unit cell models without consideration of the local Knudsen number, the coupling term determined over the unit cell and the pure gas thermal conductivity is weighted according to corrected porosities. In this particular case, decisions must therefore be made regarding the characteristic geometry both when determining the gas thermal conductivity and when designing the unit cell. Therefore, the models following now are calculated for all materials with multi scale geometry with corresponding multiple input parameters for the particle size if available, i.e. for PS and FS for the primary particle, aggregate and agglomerate size and for SG for primary particle and aggregate size.
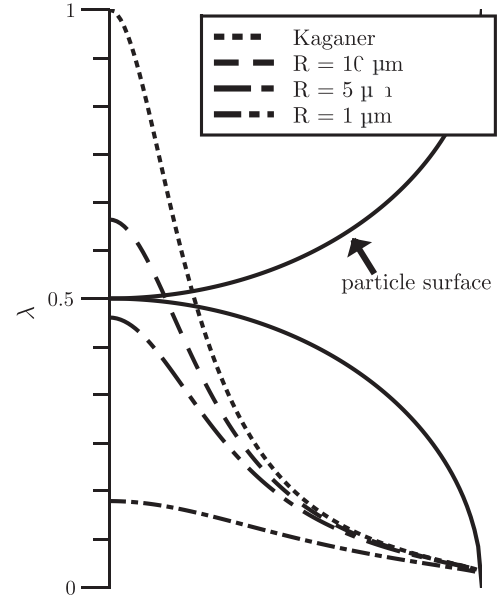
Fig. 6. Thermal conductivity progressions in a unit cell over the radius calculated with local Knudsen numbers for different particle sizes. $\lambda_p = 1\frac{W}{mK}$, λ_g calculated with Eq. (1) using the material values of air at atmospheric pressure and $\beta = 4.3$.

4.3.1. Sphere model

Swimm et al. [58] propose to calculate the thermal conductivity in a cylindrical unit cell with locally different Knudsen numbers. The unit cell is divided into a finite number of cylindrical shells and their thermal resistances are calculated as parallel connections. Since the void distance in each cylindrical shell is different, different Knudsen numbers and thus different gas thermal conductivities result. The void distance over the radius for a division into N cylinder shells for the i-th shell results in Eq. (30). Accordingly, D and R are the diameter and the radius of the primary particles, aggregates or agglomerates.

$$x(i) = D - 2\sqrt{R^2 - \left(\frac{i}{N}R\right)^2} \tag{30}$$

The area perpendicular to the heat flow of the regarding cylinder shell is $A_i = \pi(2i-1)\left(\frac{R}{N}\right)^2$. The coupling conductivity of the entire unit cell can consequently be calculated via Eq. (31), in which λ'_g is calculated as a function of $x(i)$ for every i with the respective formula from Chapter 3.

$$\lambda_c = \frac{2}{R\pi}\sum_{i=1}^{N} A_i\left(\frac{D-x(i)}{\lambda'_g} + \frac{x(i)}{\lambda_p}\right)^{-1} \tag{31}$$

To calculate the effective thermal conductivity of the bulk material, the thermal conductivity of the pure gas phase λ_g and that of the unit cell λ_c are weighted according to a corrected porosity ϕ_{corr} as shown in Eq. (32).

$$\lambda_{eff} = \lambda_{base} + \phi_{corr}\lambda_g + (1 - \phi_{corr})\lambda_c \tag{32}$$

For the spherical unit cell Eq. (23) results in Eq. (33) as it was used by the original authors.

$$\phi_{corr} = \frac{3\phi - 1}{2} \tag{33}$$

To illustrate the influence of the local Knudsen numbers, the thermal conductivity curves in a unit cell with spherical particles of different radii are shown in Fig. 6. For comparison, the curve progression with homogeneous gas thermal conductivity in the entire unit cell, as used by Kaganer, for example, is also shown.

Swimm's model was improved by Guo and Tang [37] especially for aerogels by considering an overlapping of the spheres and taking into account a coupling not only in the gap between the particles but also between particle chains and air gaps. As this is aerogel specific, it was not further investigated in this paper.

4.3.2. Zehner, Schlünder

Zehner and Schlünder [34] further developed their well-known model from [56] by also considering the Smoluchowski effect locally in the interparticle voids. For this purpose, a local Knudsen number is calculated at each location by correcting the global Knudsen number Kn to $Kn^* = \frac{Kn}{(1-x(r))}$. After integration over the radius of the unit cell λ_c can be written as shown in Eq. (34).

$$\lambda_c = \lambda_0 \frac{2}{N-M} \left\{ \frac{\left[N - (1+Kn)\frac{\lambda_0}{\lambda_p} \right] B}{(N-M)^2} \ln \frac{N}{M} \right.$$
$$\left. - \frac{B-1}{N-M}(1+Kn) - \frac{B+1}{2B}\frac{\lambda_p}{\lambda_0}[1 - (N-M) - (B-1)Kn] \right\} \quad (34)$$

with

$$M = B\left[\frac{\lambda_0}{\lambda_p} + Kn(1+Nu_r^*) \right]$$

and

$$N = (1+Nu_r^*)(1+Kn)$$

The Knudsen number occurring here can be distinguished from the Knudsen number used to calculate pure gas thermal conductivity. The particle size must be used to calculate the Knudsen number in order to adequately describe the size of the gap in which the coupling thermal conductivity occurs. For materials with a multi-scale structure, the decision between primary particle size, aggregate size and agglomerate size is again of crucial importance. Nu_r is an empirical parameter to account for the radiation. The calculation can be taken from the original literature. With the corrected porosity $1 - \sqrt{1-\phi}$ one gets Eq. (35) for the effective thermal conductivity.

$$\lambda_{eff} = (1 - \sqrt{1-\phi})(\lambda_g + \phi\lambda_0 Nu_r) + \sqrt{1-\phi}\lambda_c \quad (35)$$

4.4. Slavin

In this unit cell model from Slavin [59] the roughness of the particles is taken into account. The model treats the spheroids as being perfect spheres, separated at their contact points by a short cylinder of area d and length 2hr representing the surface roughness. In the present investigation for multi scale structures the radii of the next smaller structure was chosen as hr. For the primary particles a complete smooth surface and for the glass spheres a constant roughness of 0.1 μm was assumed. As in other models, the unit cell is divided into different regions which are then considered as parallel or in series. The gas thermal conductivity in the space between the particles is divided into an inner and an outer region. Where the regions begin and end depends on the particle size and the mean free path. In the inner region, the Smoluchowski effect is considered with a global Knudsen number. The individual calculation steps can be taken from the original literature. Eq. (36) shows the calculation of the effective thermal conductivity of the unit cell as a parallel and series connection of the individual heat resistances G_x of different parts of the unit cell.

$$\lambda_{eff} = \left\{ G_{rv} + G_{gv}\left[G_r + N_c\left(\frac{G_s(G_i + G_o + G_c)}{G_s + G_i + G_o + G_c} \right) \right] \right\} \frac{L_s}{A_{cp} + A_v} \quad (36)$$

N_c is the average effective number of contact points of a particle which is 1.5 according to Slavin et al., the height of the unit cell $L_s = \sqrt{\frac{8}{3}}R$ and A_{cp} and A_v are the area of the particle and the

void space respectively. To "fix" the low pressure conductivity and for comparability with the other models the contact resistance was set to $G_c = \lambda_{base}\frac{A_{cp}+A_v}{N_cL}$. Slavin's model does not include a classical term λ_g like the other models. Therefore, the results here do not distinguish between the calculation methods for β and the geometric size x.

5. Evaluation procedure

In order to evaluate the results obtained with the different models and calculation methods, they need to be compared with the measured ETCs. The mean-variance S of the calculated to the measured thermal conductivity values for gas pressure levels $j = 1 : N$ as shown in Eq. (37) is used for this purpose.

$$S = \frac{\sum_{j=1}^{N} \left| \frac{\lambda_m(j) - \lambda_{eff}(j)}{\lambda_m(j)} \right|}{N} \quad (37)$$

This approach results in one S value for every solid gas combination. Thus, an average of the mean-variances S for all materials and gases $\bar{S}_{all}$ can be calculated for every combination of calculation methods. For example the average variance for the sphere model in combination with Eq. (3) for β, Baules model for α and the pore size distribution + sphere correction for x. In this way a total number of 175 $\bar{S}_{all}$ values are generated for every ETC model and stored in a matrix called R_{all}. The $\bar{S}_{all}$ values provide information to assess the suitability of the models for calculating the thermal conductivity curves of any unknown silica-based porous material. In order to be able to make a statement about the suitability of the models for the calculation of individual material groups, average values of the corresponding variances $\bar{S}_{PS}, \bar{S}_{FS}, \bar{S}_{SG}$ and $\bar{S}_{GS}$ are also calculated and stored in tables R_{PS}, R_{FS}, R_{SG} and R_{GS}, respectively. A summary of the calculation steps that were performed for the evaluation using a MATLAB (Co. The MathWorks Ink.) calculation program is shown below. The entire code for one exemplary ETC model is provided as supplementary material.

```
for D_part = [D_aggl; D_aggr; D_prim]
  for α = [Eq. (7) : Eq. (11)]
    for β = [Eq. (2) : Eq. (6)]
      for λ_g = f(x) - Six options for x (see Table 5)
        for m = 1 : N (N = 15 materials)
          for i = 1 : J (J = 7 gases)
            λ_eff = [Eq. (17), (18), (20), (21), (25), (27), (29),
                     (32), (34), (36)]
            S = [Eq. 37]
          end
          S̄ = ΣS(m,i)/(N*J)
        end
      end
    end
  end
```

$$R_{all}, R_{PS}, R_{FS}, R_{SG}, R_{GS} = \begin{bmatrix} \bar{S}_{1,1} & \cdots & \cdots \\ \vdots & \ddots & \vdots \\ \cdots & \cdots & \bar{S}_{7,25} \end{bmatrix}$$

For each effective thermal conductivity model a total of five matrices R are calculated, each with 175 $\bar{S}$ values, one with mean values for all tested materials and four more for each material class (PS, FS, SG, GS). Each matrix consists of 7 x 25 mean-variances $\bar{S}$ which were determined using the described combination of calculation methods. The lowest mean-variance in each case indicates the best-suited combination for the corresponding material class.

6. Results and discussion

After calculating the thermal conductivity progressions for all porous medium-gas combinations with all mentioned combinations of equations for α, β and x, the variances $\overline{S}$ (or matrices R) were summarized in tables, which are accordingly available as supplementary material. The smaller the $\overline{S}$ value, the better the respective combination of calculation models works for the corresponding class of materials (PS, FS, SG, GS) or, in the case of $\overline{S_{all}}$, for the totality of all materials. The best three combinations for each ETC model were extracted and are called "favorites" in the following. The lists of favorites for all material classes are shown in the appendix in Tables B.1–B.5. To get an additional overview of which GTC models lead to the most promising results in general, mean values of all variances which have been calculated with the different models for α, β and x are shown in Table 6. There is one row for the totality of all materials and one for every material class. Since all model combinations which include the respective GTC models have been taken into account for the calculation of the mean variances the absulut values are very high. But even if influences of the "good" as well as of the "worse" ETC-models can be found here, it serves as an adequate measure to compare the influences of the calculation methods for α, β and x. The difference between them, on the other hand, allows a statement to be made about which GTC model provides good results for which material class with the highest probability. On the other hand, the spread of the data can be used to make a qualitative statement about the sensitivity of the results to the different GTC models. The greater the spread, the more important it is to choose the right model in the corresponding category.

The compilation in Table 6 shows that in general it seems reasonable to use one of the older models, e.g. Baule's or Goodman's for the calculation of the TAC. These models predict significantly smaller TACs than the newer ones (Fig. 2). This finding does not allow any statement about the actual thermal accommodation coefficients between a silica surface and the different gases. Only a recommendation for the calculation of the gas thermal conductivity can be given here. The hypothesis that either recent literature classifies TACs fundamentally too high (which is not suspected by the authors) or that an adjustment is necessary in some common models for the calculation of the gas thermal conductivity, is supported by the findings of our previous work [45], which indicates

lower TACs as well. Taking into account that recent measurements or simulations from the literature regarding the TAC [60,61] are more in line with the newer models of e.g. Bauer or Song it can be assumed that they are more physically correct than the older ones even though they seem to have more accordance in the current investigation.

The best equations to calculate the dimensionless parameter β are Eq. (2) and Eq. (6). They differ only slightly and lead to the highest β-values as is shown in Fig. 1. In contrast, there is exactly a factor of 0.5 between Eq. (2) and Eq. (3). Interestingly, Eq. (3) occurs particularly often in the favorites in combination with the newer models for α. This reinforces the tendency to even lower β-values and therefore higher gas thermal conductivities. This combination occurs strikingly often for PS. A possible explanation for this is a higher concentration of silanol groups on the surface of PS compared to FS for example and potentially the clear different particle shape. Silanol groups affect the molar mass of the surface layer, by which the gas molecules collide, and thus the energy accommodation between them. Different pore shapes or roughness can have many effects on the thermal conductivity like multiple molecule collisions, changes of the mean free distance of gas molecules, or of the coupling effect.

As expected, it is advisable to calculate the gas thermal conductivity with the help of the pore size distribution and Eq. (13), if corresponding data are available. Additionally, it can be recommended for most materials to use the correction from Eq. (15). If no measured data of the pore size distribution are available, the Kozeny correction can be applied as described. It is essential to ensure that in this case the aggregate size is used for PS and the primary particle size for FS or SG. For precipitated as well as fumed silica this procedure seems to be even more promising than the use of the pore size distribution. However, the results shown in Table 6 only indicate a rough trend and must not be overestimated. The results may be overlaid by other influencing parameters and do not necessarily coincide with the actual model combinations to be favored for the different material classes as described below. In the following subsections Fig. 7 shows the measured data for all materials investigated in comparison to the calculated results of the model combination, which fitted best on the over all average. Figs. 8 to 11 show the same measured values in comparison to the favorite model combination for the different individual material classes.

6.1. All materials

The best results for all porous materials on average were achieved with the Sphere ETC model with consideration of the local Knudsen number (Section 4.3.1) in combination with Bauer's model for α, Eq. (6) for β and the pore size distribution without correction as the geometric size. Thus, if the material of interest is from unknown nature or if a material is involved that was not examined in this study, this model combination leads to the most promising results. In this case the aggregate size should be used as the geometric size parameter of the unit cell of the sphere model. The calculated values have a mean-variance of 18.5% to the measurements and are shown in Fig. 7 together with the measured values.

6.2. Precipitated silica

The measurement results of precipitated silica were also best obtained by the sphere model with consideration of local Knudsen numbers as it was presented by Swimm et al. (Section 4.3.1). The local Knudsen number in the sphere model is best calculated using the agglomerate size in case of PS. However, for the determination of the gas thermal conductivity, the simple calculation via the peak

Table 6
Average variances which were obtained with the calculation methods for α, β and the geometric size in percent.

	all	PS	FS	SG	GS
α					
Baule	46.8	38.6	51.6	40.3	64.7
Goodman	48.4	39.0	53.5	41.4	69.2
Kaganer	55.4	40.5	60.8	45.7	89.1
Song	56.6	41.2	63.0	46.9	90.6
Bauer	59.0	41.9	65.5	48.6	96.7
β					
Eq. (2)	50.5	39.5	55.6	42.7	75.0
Eq. (3)	57.0	41.1	62.8	46.9	92.8
Eq. (4)	55.1	40.8	61.1	45.8	86.8
Eq. (5)	52.9	40.3	59.1	44.5	80.3
Eq. (6)	50.7	39.5	55.7	42.8	75.4
x					
d_{peak}	46.0	36.2	34.2	40.1	82.8
d_{dist}	42.2	29.0	37.9	31.2	83.4
$d_{peak} * \frac{\pi}{6}$	43.9	37.5	34.9	40.4	69.0
$d_{dist} * \frac{\pi}{6}$	38.2	29.8	31.1	30.8	69.4
D_{aggl} + KC	107.5	84.2	214.6		
D_{aggr} + KC	48.9	29.2	31.7	64.1	
D_{prim} + KC	46.1	35.7	27.6	41.1	89.9

Fig. 7. Results of the best model combination to forecast thermal conductivity over pressure progressions (solid lines) and according to measurement results (asterisks) for an arbitrary silica material.
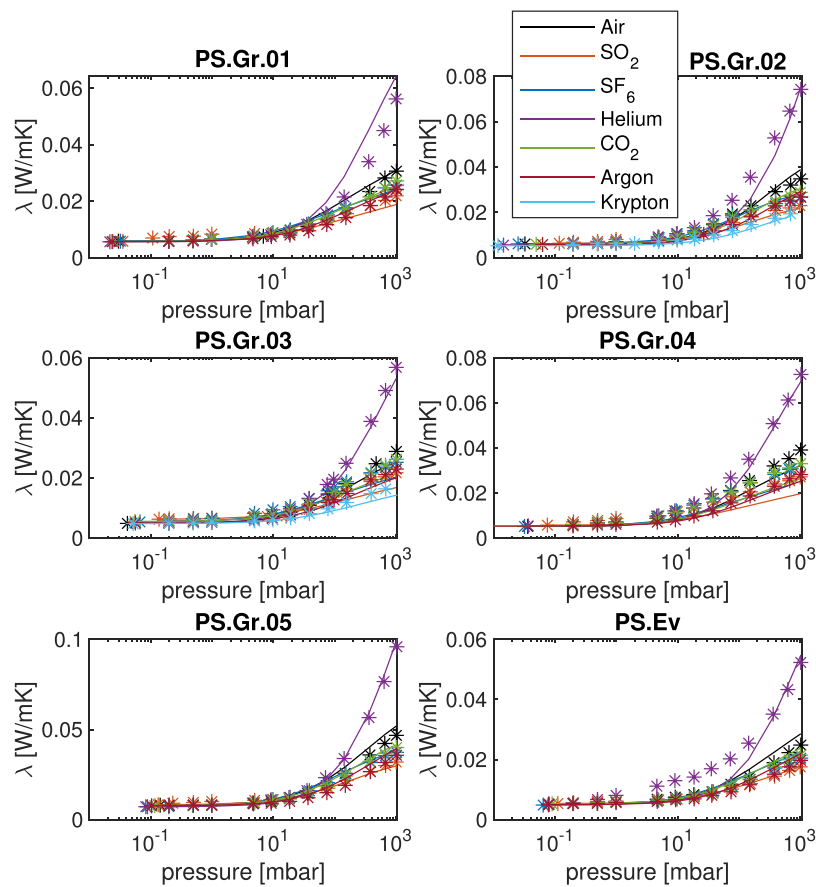
Fig. 8. Results of the best model combination to forecast precipitated silica thermal conductivity over pressure progressions (solid lines) and according to measurement results (asterisks).

of the mercury intrusion porosimetry measurements together with the formula from Bauer for α and Eq. (4) for β is suitable. This is one of the very few examples where the use of the peak size was convincing. If the pore size distribution with correction is used instead, the mean-variance is only 0.07% worse. Since the assumption suggests that the good performance of the peak size could be incidental, the use of the pore size distribution can also be recommended instead. Thus, a mean accuracy of 10.6% can be obtained for forecasting the thermal conductivity progression of precipitated silica as it is shown in Fig. 8.
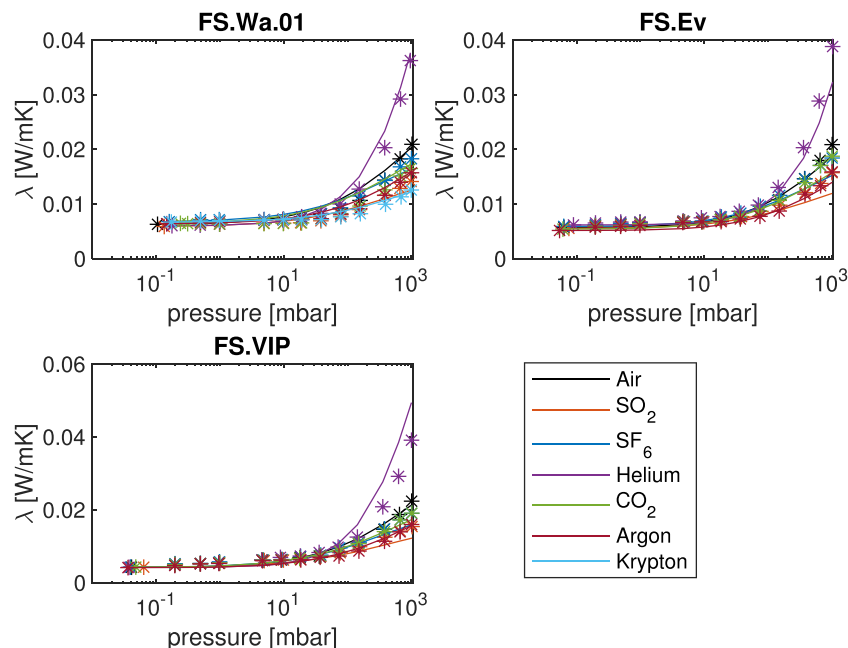
Fig. 9. Results of the best model combination to forecast fumed silica thermal conductivity over pressure progressions (solid lines) and according measurement results (asterisks).
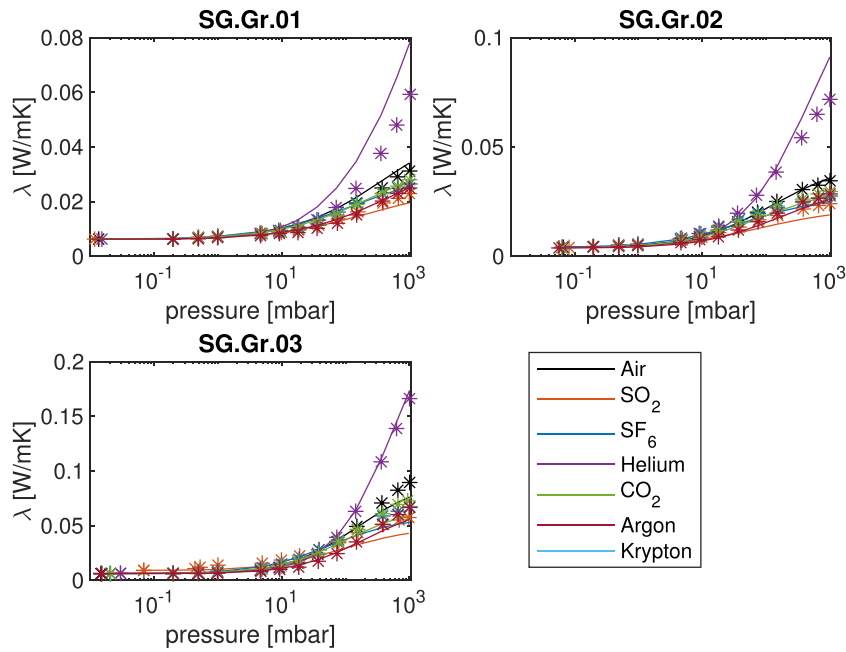
Fig. 10. Results of the best model combination to forecast silica gel thermal conductivity over pressure progressions (solid lines) and according to measurement results (asterisks).

6.3. Fumed silica

The thermal conductivity progressions of fumed silica can be predicted by many models with a very good accuracy. In the favorites, the $\overline{S_{FS}}$ value is mostly around 10%. There is a very clear tendency to Baule's and Goodman's models for α, Eq. (2) and Eq. (6) for β as well as the pore size distribution with correction for x. However, the very best result was achieved with the Kaganer's model for α, Eq. (2) for β and the pore size distribution for x in combination with the new model from Zehner and Schlünder (Section 4.3.2) and the aggregate size for the calculation of the local Knudsen number in the unit cell. This combination leads to

the mean-variance of 9.2%. The respective progressions are plotted in Fig. 9.

6.4. Silica gel

An even more accurate prediction than with fumed silica could only be achieved with silica gel. Although most of the $\overline{S_{SG}}$ values in the favorites are closer to 15%, the smallest value was just 8.7%. That is the most precise combination of prediction methodes of the whole investigation. It was obtained, like for PS, by the sphere model with consideration of the local Knudsen number (Section 4.3.1). However, this time it was the aggregate size that
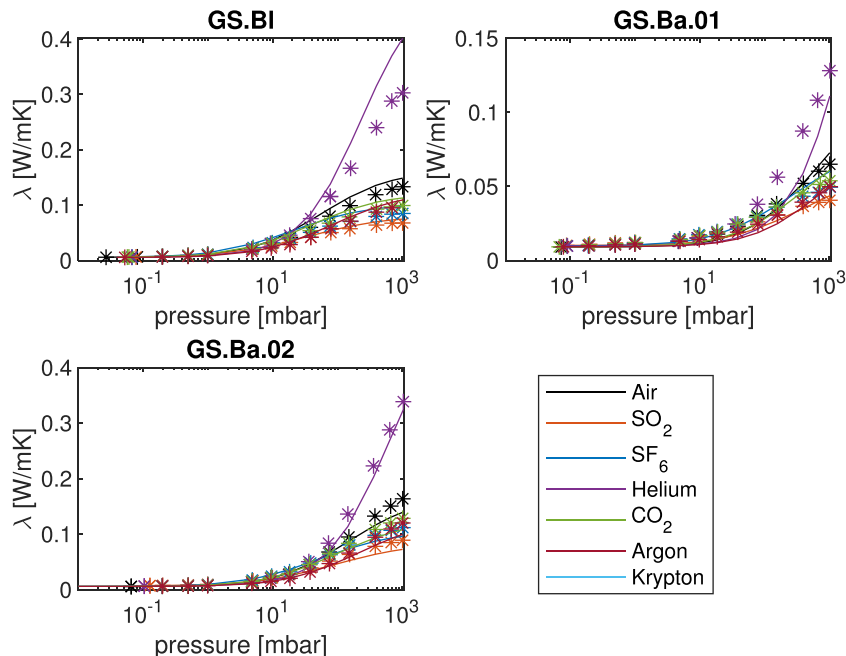
Fig. 11. Results of the best model combination to forecast glass spheres thermal conductivity over pressure progressions (solid lines) and according to measurement results (asterisks).
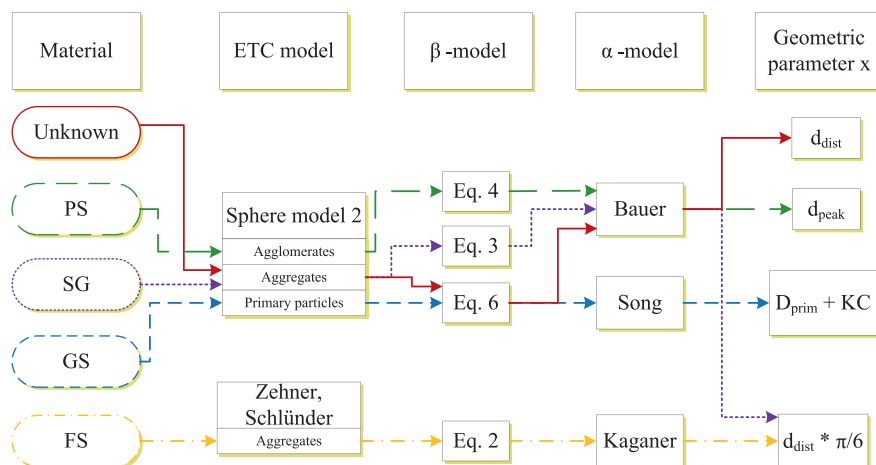
Fig. 12. Flowchart for the selection of models to calculate effective thermal conductivity of different silica based porous materials.

was most suitable for the calculation of the local Knudsen number, not the agglomerate size. However, this is due to the fact that this size scale does not exist for silica gels. Therefore, it is also the "largest particles" that should be used for the calculation with the sphere model.

6.5. Glass spheres

Surprisingly, glass spheres have turned out to be the most unpredictable material class in terms of ETC, although the porous media offer the seemingly most straightforward structure. Best results could be obtained again with the sphere model from Section 4.3.1. This is not surprising, because the spherical shape of the unit cell fits very well to the original shape of the particles. The sphere model delivers the best results in combination with Eq. (6) for β, Song's model for α and the particle size with Kozeny's correction for the calculation of the GTC. Results are shown in Fig. 11 accordingly.

7. Conclusion

In the present study, 15 porous media which are all based on silicon dioxide have been characterized in terms of pressure-dependent thermal conductivity in combination with 7 different gases each. Furthermore, the structural properties of the materials have been investigated. Pore size distributions were measured with mercury intrusion porosimetry and particle sizes with small angle x-ray scattering, dynamic light scattering, laser diffraction and digital light microscopy. Ten popular analytical models from the literature to calculate the effective thermal conductivity of porous media are presented and categorized as follows: Geometry independent models, unit cell models and unit cell models with consideration of local Knudsen numbers. Additionally, several models to calculate the gas thermal conductivity in the pores of the materials have been presented. Altogether the study results in 2800 possible combinations which have been examined using a Matlab code and compared with the measurements. The crucial finding of the paper is probably that basically all models promise better accuracy than is achieved in practice with the real measurement data presented. This is not surprising, because most of the models have been created for special material groups or with regard to some other measured data. The effective thermal conductivity of an unknown porous silica material with an arbitrary Knudsen gas inside of the pores can be forecasted with an average accuracy of about 18.5%, using the sphere model with consideration of the local Knudsen number. In conclusion, this rather compli-

cated model, which requires the use of a computer performs best on the overall average. But, also the simple models presented by Russel or Maxwell still deliver an acceptable overall variance of about 20%. However, it turns out that it is helpful to know about the material class, because by selecting a suitable GTC and ETC model combination, a significantly smaller average error of about 10% can be achieved. More precisely, for the material classes PS, FS, SG and GS minimum average errors of 10.5%, 9.2%, 8.7% and 11.9% could be obtained, respectively. In all cases it was a unit cell ETC model with consideration of the local Knudsen number which performed best. The size scale of the unit cell should be taken from the largest particle size scale for PS, SG and GS. That means agglomerate size for PS, aggregate size for SG and the simple (primary) particle size for GS. One exception is FS, which is best calculated using the aggregate size, even though FS tends to form large agglomerates. The size scale that is decisive for the heat transport does not seem to be that of the agglomerates but that of the aggregates. This behavior can be explained by the unusual structure of FS and makes clear why fumed silica is usually preferred in the production of vacuum insulation panels instead of the cheaper precipitated silica, despite similar porosity and particle size. In most of the cases it can be recommended to use the pore size distribution to calculate the gas thermal conductivity if it is available. Additionally, it can be helpful to use the pore size correction which is shown in Eq. (15) in some cases. If the pore size distribution is not available, the particle size with Kozeny's correction (Eq. 14) can be used instead. If so, it is advisable to use the aggregate size for PS and the primary particle size for FS and SG.

The study has shown that different models for calculating thermal conductivities have their justification because different models fit best for different materials. Fig. 12 shows a scheme for one potential selection of models for different silica based materials recommended by the authors of the study. If one follows the advice given in this paper, gas pressure-dependent thermal conductivities of silica-based porous materials can be predicted with fairly good accuracy in most cases. The knowledge can be used in the development of new thermal insulation or in all other areas where the thermal conductivity of porous media in combination with a Knudsen gas is of interest.

Declaration of Competing Interest

The authors declare that they have no known competing financial interests or personal relationships that could have appeared to influence the work reported in this paper.

Acknowledgments

Appendix A. Pore size distributions

Taking a closer look at the pore size distributions which are shown in Fig. A.1 one can see the different pore structures of the materials. It is evident that different materials, even from the same material group, can show a significant difference in the position of the pore peak even if porosity and thermal conductivity only differ slightly. In the case of PS two samples (PS.Gr.02 and PS.Gr.05) show a peak in the size scale of the aggregates and the other four in the primary particle size scale. Nevertheless, they do not have much in common in terms of porosity or thermal conductivity. This shows that it can lead to inaccuracies to use the peak size only for the calculation of the GTC. Instead, the whole distribution should be taken into account if possible. Furthermore, the narrow distribution of the glass beads is striking. From this, it can be seen that the pile structure is fundamentally different from the other materials.
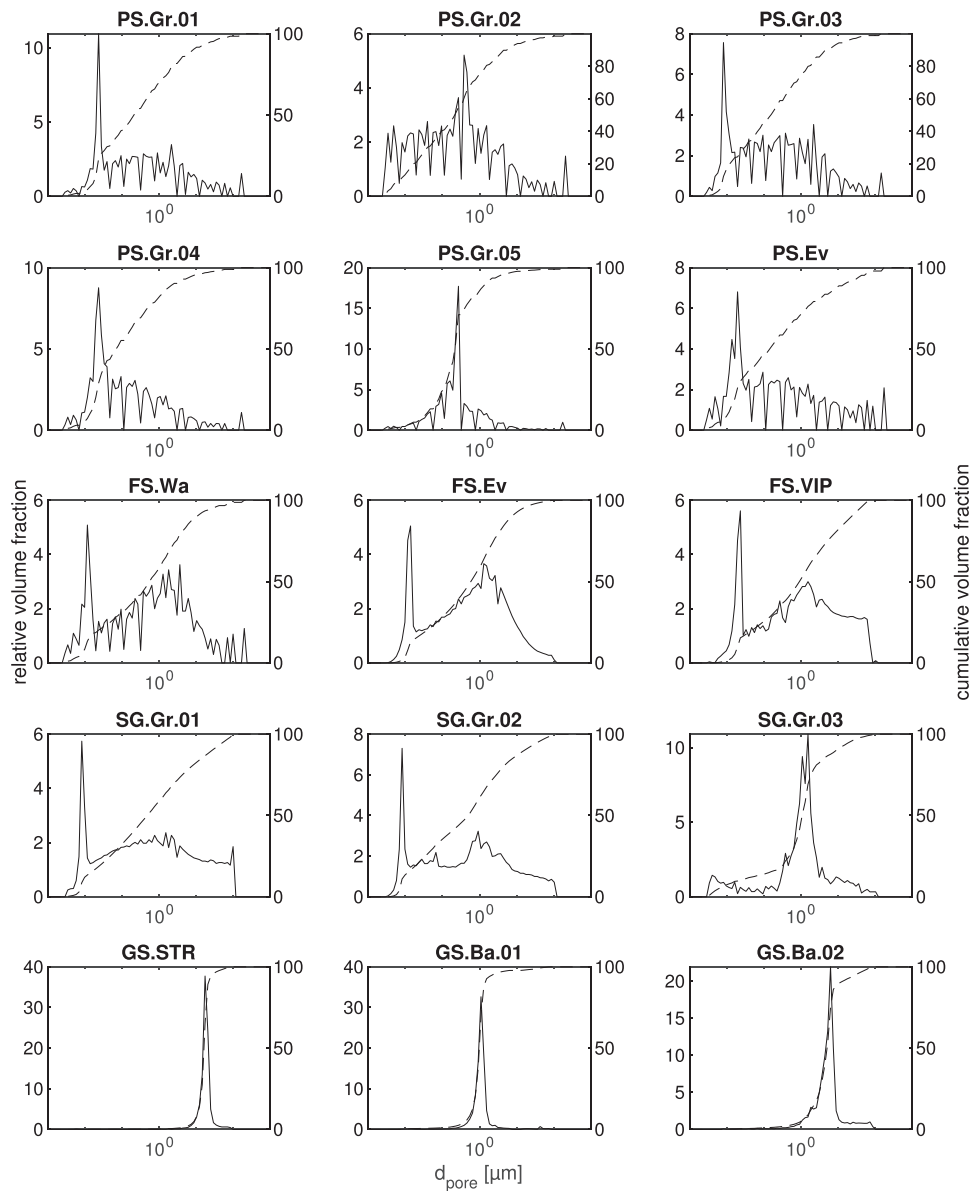
Fig. A1. Pore size distributions of all materials investigated, measured with mercury intrusion porosimetry. The primary and secondary axes represent the relative and the cumulative volume fraction and are plotted in solid and dashed lines respectively. The x-axis shows the pore sizes in μm.

15

Appendix B. Favorites of model combinations

Table B1
Over all favorites - three GTC model combinations with the lowest $\overline{S_{all}}$ values for every ETC model.

		α	β	x	$\overline{S_{all}}$
Russel	1	Goodman	Eq. (5)	$d_{dist} * \frac{\pi}{6}$	0.2003
	2	Goodman	Eq. (4)	$d_{dist} * \frac{\pi}{6}$	0.2012
	3	Baule	Eq. (2)	d_{dist}	0.2014
Maxwell	1	Song	Eq. (2)	$d_{dist} * \frac{\pi}{6}$	0.2092
	2	Song	Eq. (6)	$d_{dist} * \frac{\pi}{6}$	0.2092
	3	Baule	Eq. (5)	d_{dist}	0.2095
Scaling Model	1	Baule	Eq. (6)	$d_{dist} * \frac{\pi}{6}$	0.2206
	2	Baule	Eq. (2)	$d_{dist} * \frac{\pi}{6}$	0.2207
	3	Goodman	Eq. (2)	$d_{dist} * \frac{\pi}{6}$	0.2223
Sphere model 1	1	Baule	Eq. (5)	$d_{dist} * \frac{\pi}{6}$	0.2476
	2	Baule	Eq. (4)	$d_{dist} * \frac{\pi}{6}$	0.2480
	3	Goodman	Eq. (5)	$d_{dist} * \frac{\pi}{6}$	0.2488
Schumann and Voss	1	Baule	Eq. (5)	$d_{dist} * \frac{\pi}{6}$	0.2132
	2	Baule	Eq. (4)	$d_{dist} * \frac{\pi}{6}$	0.2139
	3	Goodman	Eq. (5)	$d_{dist} * \frac{\pi}{6}$	0.2166
Luikov	1	Baule	Eq. (2)	$d_{dist} * \frac{\pi}{6}$	0.4382
	2	Baule	Eq. (6)	$d_{dist} * \frac{\pi}{6}$	0.4427
	3	Goodman	Eq. (2)	$d_{dist} * \frac{\pi}{6}$	0.5018
Zehner, Bauer, Schlünder	1	Baule	Eq. (6)	$d_{dist} * \frac{\pi}{6}$	0.2667
	2	Baule	Eq. (2)	$d_{dist} * \frac{\pi}{6}$	0.2669
	3	Goodman	Eq. (2)	$d_{dist} * \frac{\pi}{6}$	0.2670
Sphere model 2 primary particles	1	Kaganer	Eq. (5)	d_{dist}	0.2285
	2	Bauer	Eq. (2)	d_{dist}	0.2287
	3	Bauer	Eq. (6)	d_{dist}	0.2287
Sphere model 2 aggregates	1	Bauer	Eq. (6)	d_{dist}	0.1849
	2	Kaganer	Eq. (5)	d_{dist}	0.1850
	3	Bauer	Eq. (2)	d_{dist}	0.1851
Sphere model 2 agglomerate	1	Bauer	Eq. (6)	d_{peak}	0.1860
	2	Bauer	Eq. (2)	d_{peak}	0.1863
	3	Kaganer	Eq. (5)	d_{peak}	0.1870
Zehner, Schlünder primary particles	1	Kaganer	Eq. (3)	d_{dist}	0.3608
	2	Bauer	Eq. (3)	d_{dist}	0.3629
	3	Song	Eq. (3)	d_{dist}	0.3630
Zehner, Schlünder aggregates	1	Kaganer	Eq. (2)	d_{dist}	0.3272
	2	Kaganer	Eq. (6)	d_{dist}	0.3273
	3	Kaganer	Eq. (3)	$d_{dist} * \frac{\pi}{6}$	0.3274
Zehner, Schlünder agglomerate	1	Kaganer	Eq. (2)	d_{peak}	0.4790
	2	Kaganer	Eq. (6)	d_{peak}	0.4790
	3	Kaganer	Eq. (3)	$d_{peak} * \frac{\pi}{6}$	0.4790
Slavin primary particles	1	Baule		d_{peak}	0.6675
	2	Baule		d_{dist}	0.6675
	3	Baule		$d_{peak} * \frac{\pi}{6}$	0.6675
Slavin aggregates	1	Baule		d_{peak}	0.4759
	2	Baule		d_{dist}	0.4759
	3	Baule		$d_{peak} * \frac{\pi}{6}$	0.4759
Slavin agglomerate	1	Baule		d_{peak}	0.5151
	2	Baule		d_{dist}	0.5151
	3	Baule		$d_{peak} * \frac{\pi}{6}$	0.5151

Table B2

Precipitated silica favorites - three GTC model combinations with the lowest $\overline{S_{PS}}$ values for every ETC model.

		α	β	x	$\overline{S_{PS}}$
Russel	1	Kaganer	Eq. (4)	d_{dist}	0.1567
	2	Bauer	Eq. (5)	D_{aggr} + KC	0.1581
	3	Kaganer	Eq. (3)	d_{dist}	0.1583
Maxwell	1	Bauer	Eq. (3)	D_{aggr} + KC	0.1432
	2	Song	Eq. (3)	D_{aggr} + KC	0.1507
	3	Bauer	Eq. (4)	D_{aggr} + KC	0.1511
Scaling Model	1	Goodman	Eq. (3)	d_{dist}	0.1551
	2	Kaganer	Eq. (4)	$d_{dist} * \frac{\pi}{6}$	0.1558
	3	Goodman	Eq. (4)	d_{dist}	0.1561
Sphere model 1	1	Bauer	Eq. (3)	D_{aggr} + KC	0.1415
	2	Bauer	Eq. (4)	D_{aggr} + KC	0.1524
	3	Song	Eq. (3)	D_{aggr} + KC	0.1528
Schumann and Voss	1	Bauer	Eq. (5)	D_{aggr} + KC	0.1403
	2	Song	Eq. (4)	D_{aggr} + KC	0.1423
	3	Song	Eq. (5)	D_{aggr} + KC	0.1467
Luikov	1	Baule	Eq. (2)	$d_{dist} * \frac{\pi}{6}$	0.1927
	2	Baule	Eq. (6)	$d_{dist} * \frac{\pi}{6}$	0.1941
	3	Goodman	Eq. (2)	$d_{dist} * \frac{\pi}{6}$	0.2130
Zehner, Bauer, Schlünder	1	Bauer	Eq. (4)	D_{aggr} + KC	0.1382
	2	Bauer	Eq. (3)	D_{aggr} + KC	0.1407
	3	Song	Eq. (3)	D_{aggr} + KC	0.1416
Sphere model 2	1	Bauer	Eq. (3)	D_{aggr} + KC	0.2140
primary particles	2	Song	Eq. (3)	D_{aggr} + KC	0.2283
	3	Bauer	Eq. (4)	D_{aggr} + KC	0.2290
Sphere model 2	1	Bauer	Eq. (3)	D_{aggr} + KC	0.1954
aggregates	2	Bauer	Eq. (3)	d_{dist}	0.2062
	3	Song	Eq. (3)	D_{aggr} + KC	0.2101
Sphere model 2	1	Bauer	Eq. (4)	d_{peak}	0.1051
agglomerate	2	Bauer	Eq. (3)	$d_{peak} * \frac{\pi}{6}$	0.1058
	3	Bauer	Eq. (3)	d_{peak}	0.1064
Zehner, Schlünder	1	Baule	Eq. (2)	D_{aggl} + KC	0.2073
primary particles	2	Baule	Eq. (6)	D_{aggl} + KC	0.2089
	3	Goodman	Eq. (2)	D_{aggl} + KC	0.2280
Zehner, Schlünder	1	Bauer	Eq. (3)	D_{aggr} + KC	0.1908
aggregates	2	Bauer	Eq. (3)	d_{dist}	0.1952
	3	Song	Eq. (3)	D_{aggr} + KC	0.1998
Zehner, Schlünder	1	Kaganer	Eq. (3)	d_{peak}	0.2904
agglomerate	2	Kaganer	Eq. (4)	d_{peak}	0.2914
	3	Song	Eq. (3)	d_{peak}	0.2916
Slavin	1	Bauer		d_{peak}	0.4384
primary particles	2	Bauer		d_{dist}	0.4384
	3	Bauer		$d_{peak} * \frac{\pi}{6}$	0.4384
Slavin	1	Bauer		d_{peak}	0.4294
aggregates	2	Bauer		d_{dist}	0.4294
	3	Bauer		$d_{peak} * \frac{\pi}{6}$	0.4294
Slavin	1	Baule		d_{peak}	0.4805
agglomerate	2	Baule		d_{dist}	0.4805
	3	Baule		$d_{peak} * \frac{\pi}{6}$	0.4805

Table B3
Fumed silica favorites - three GTC model combinations with the lowest $\overline{S_{FS}}$ values for every ETC model.

		α	β	x	$\overline{S_{FS}}$
Russel	1	Baule	Eq. (2)	$d_{dist} * \frac{\pi}{6}$	0.1020
	2	Baule	Eq. (6)	$d_{dist} * \frac{\pi}{6}$	0.1032
	3	Goodman	Eq. (2)	$d_{dist} * \frac{\pi}{6}$	0.1221
Maxwell	1	Baule	Eq. (5)	$d_{dist} * \frac{\pi}{6}$	0.0944
	2	Goodman	Eq. (6)	$d_{dist} * \frac{\pi}{6}$	0.0945
	3	Goodman	Eq. (2)	$d_{dist} * \frac{\pi}{6}$	0.0949
Scaling Model	1	Baule	Eq. (2)	$d_{dist} * \frac{\pi}{6}$	0.1119
	2	Baule	Eq. (6)	$d_{dist} * \frac{\pi}{6}$	0.1130
	3	Bauer	Eq. (5)	$D_{prim} + KC$	0.1228
Sphere model 1	1	Baule	Eq. (5)	$d_{dist} * \frac{\pi}{6}$	0.0951
	2	Baule	Eq. (2)	d_{dist}	0.0957
	3	Goodman	Eq. (5)	$d_{dist} * \frac{\pi}{6}$	0.0959
Schumann and Voss	1	Baule	Eq. (2)	$d_{dist} * \frac{\pi}{6}$	0.0951
	2	Baule	Eq. (6)	$d_{dist} * \frac{\pi}{6}$	0.0958
	3	Goodman	Eq. (2)	$d_{dist} * \frac{\pi}{6}$	0.1090
Luikov	1	Baule	Eq. (5)	$D_{prim} + KC$	0.1363
	2	Baule	Eq. (4)	$D_{prim} + KC$	0.1369
	3	Goodman	Eq. (6)	$D_{prim} + KC$	0.1396
Zehner, Bauer, Schlünder	1	Goodman	Eq. (6)	$d_{dist} * \frac{\pi}{6}$	0.0931
	2	Goodman	Eq. (2)	$d_{dist} * \frac{\pi}{6}$	0.0932
	3	Baule	Eq. (5)	$d_{dist} * \frac{\pi}{6}$	0.0960
Sphere model 2	1	Goodman	Eq. (3)	$d_{dist} * \frac{\pi}{6}$	0.1038
primary particles	2	Song	Eq. (2)	$d_{dist} * \frac{\pi}{6}$	0.1041
	3	Kaganer	Eq. (6)	$d_{dist} * \frac{\pi}{6}$	0.1041
Sphere model 2	1	Kaganer	Eq. (6)	$d_{dist} * \frac{\pi}{6}$	0.0988
aggregates	2	Goodman	Eq. (3)	$d_{dist} * \frac{\pi}{6}$	0.0989
	3	Kaganer	Eq. (2)	$d_{dist} * \frac{\pi}{6}$	0.0992
Sphere model 2	1	Baule	Eq. (2)	d_{peak}	0.1187
agglomerate	2	Baule	Eq. (2)	$d_{peak} * \frac{\pi}{6}$	0.1188
	3	Baule	Eq. (6)	d_{peak}	0.1198
Zehner, Schlünder	1	Baule	Eq. (3)	d_{dist}	0.0986
primary particles	2	Kaganer	Eq. (4)	$d_{dist} * \frac{\pi}{6}$	0.1003
	3	Kaganer	Eq. (5)	$d_{dist} * \frac{\pi}{6}$	0.1004
Zehner, Schlünder	1	Kaganer	Eq. (2)	$d_{dist} * \frac{\pi}{6}$	0.0919
aggregates	2	Kaganer	Eq. (6)	$d_{dist} * \frac{\pi}{6}$	0.0920
	3	Goodman	Eq. (3)	$d_{dist} * \frac{\pi}{6}$	0.0928
Zehner, Schlünder	1	Song	Eq. (3)	d_{peak}	0.7584
agglomerate	2	Kaganer	Eq. (3)	d_{peak}	0.7585
	3	Bauer	Eq. (3)	d_{peak}	0.7588
Slavin	1	Bauer		d_{peak}	0.3411
primary particles	2	Bauer		d_{dist}	0.3411
	3	Bauer		$d_{peak} * \frac{\pi}{6}$	0.3411
Slavin	1	Bauer		d_{peak}	0.3345
aggregates	2	Bauer		d_{dist}	0.3345
	3	Bauer		$d_{peak} * \frac{\pi}{6}$	0.3345
Slavin	1	Baule		d_{peak}	0.5514
agglomerate	2	Baule		d_{dist}	0.5514
	3	Baule		$d_{peak} * \frac{\pi}{6}$	0.5514

Table B4
Silica gel favorites - three GTC model combinations with the lowest $\overline{S_{SG}}$ values for every ETC model.

		α	β	x	$\overline{S_{SG}}$
Russel	1	Kaganer	Eq. (5)	d_{dist}	0.1567
	2	Song	Eq. (3)	$d_{dist} * \frac{\pi}{6}$	0.1573
	3	Song	Eq. (6)	d_{dist}	0.1580
Maxwell	1	Kaganer	Eq. (3)	d_{dist}	0.1779
	2	Song	Eq. (3)	d_{dist}	0.1798
	3	Kaganer	Eq. (4)	d_{dist}	0.1834
Scaling Model	1	Goodman	Eq. (2)	d_{dist}	0.1317
	2	Goodman	Eq. (6)	d_{dist}	0.1319
	3	Goodman	Eq. (3)	$d_{dist} * \frac{\pi}{6}$	0.1322
Sphere model 1	1	Kaganer	Eq. (5)	d_{dist}	0.1919
	2	Kaganer	Eq. (4)	d_{dist}	0.1922
	3	Song	Eq. (3)	$d_{dist} * \frac{\pi}{6}$	0.1931
Schumann and Voss	1	Kaganer	Eq. (3)	$d_{dist} * \frac{\pi}{6}$	0.1654
	2	Kaganer	Eq. (6)	d_{dist}	0.1656
	3	Kaganer	Eq. (2)	d_{dist}	0.1659
Luikov	1	Baule	Eq. (2)	$d_{dist} * \frac{\pi}{6}$	0.1565
	2	Baule	Eq. (6)	$d_{dist} * \frac{\pi}{6}$	0.1584
	3	Goodman	Eq. (2)	$d_{dist} * \frac{\pi}{6}$	0.1910
Zehner, Bauer, Schlünder	1	Kaganer	Eq. (3)	$d_{dist} * \frac{\pi}{6}$	0.1762
	2	Kaganer	Eq. (6)	d_{dist}	0.1767
	3	Goodman	Eq. (3)	d_{dist}	0.1768
Sphere model 2	1	Baule	Eq. (2)	D_{aggl} + KC	0.2528
primary particles	2	Baule	Eq. (2)	D_{aggr} + KC	0.2528
	3	Baule	Eq. (6)	D_{aggl} + KC	0.2542
Sphere model 2	1	Bauer	Eq. (3)	$d_{dist} * \frac{\pi}{6}$	0.0867
aggregates	2	Song	Eq. (3)	$d_{dist} * \frac{\pi}{6}$	0.0901
	3	Song	Eq. (3)	d_{dist}	0.0906
Sphere model 2 agglomerate					
Zehner, Schlünder	1	Baule	Eq. (2)	D_{aggl} + KC	0.2419
primary particles	2	Baule	Eq. (2)	D_{aggr} + KC	0.2419
	3	Baule	Eq. (6)	D_{aggr} + KC	0.2424
Zehner, Schlünder	1	Kaganer	Eq. (3)	D_{prim} + KC	0.2315
aggregates	2	Bauer	Eq. (3)	D_{prim} + KC	0.2315
	3	Song	Eq. (3)	D_{prim} + KC	0.2334
Zehner, Schlünder agglomerate					
Slavin	1	Bauer		d_{peak}	0.4889
primary particles	2	Bauer		d_{dist}	0.4889
	3	Bauer		$d_{peak} * \frac{\pi}{6}$	0.4889
Slavin	1	Baule		d_{peak}	0.5983
aggregates	2	Baule		d_{dist}	0.5983
	3	Baule		$d_{peak} * \frac{\pi}{6}$	0.5983
Slavin agglomerate					

Table B5

Glass spheres favorites - three GTC model combinations with the lowest $\overline{S_{GS}}$ values for every ETC model.

		α	β	x	$\overline{S_{GS}}$
Russel	1	Baule	Eq. (5)	$d_{dist} * \frac{\pi}{6}$	0.1450
	2	Baule	Eq. (4)	$d_{dist} * \frac{\pi}{6}$	0.1482
	3	Goodman	Eq. (5)	$d_{dist} * \frac{\pi}{6}$	0.1511
Maxwell	1	Baule	Eq. (2)	D_{aggl} + KC	0.1274
	2	Baule	Eq. (2)	D_{aggr} + KC	0.1274
	3	Baule	Eq. (2)	D_{prim} + KC	0.1274
Scaling Model	1	Baule	Eq. (2)	$d_{dist} * \frac{\pi}{6}$	0.3123
	2	Baule	Eq. (6)	$d_{dist} * \frac{\pi}{6}$	0.3158
	3	Baule	Eq. (2)	$d_{peak} * \frac{\pi}{6}$	0.3387
Sphere model 1	1	Baule	Eq. (2)	$d_{dist} * \frac{\pi}{6}$	0.2121
	2	Baule	Eq. (6)	$d_{dist} * \frac{\pi}{6}$	0.2144
	3	Baule	Eq. (2)	$d_{peak} * \frac{\pi}{6}$	0.2212
Schumann and Voss	1	Baule	Eq. (2)	$d_{dist} * \frac{\pi}{6}$	0.1954
	2	Baule	Eq. (6)	$d_{dist} * \frac{\pi}{6}$	0.1973
	3	Baule	Eq. (2)	$d_{peak} * \frac{\pi}{6}$	0.2017
Luikov	1	Baule	Eq. (2)	$d_{peak} * \frac{\pi}{6}$	1.3121
	2	Baule	Eq. (6)	$d_{peak} * \frac{\pi}{6}$	1.3258
	3	Baule	Eq. (2)	$d_{dist} * \frac{\pi}{6}$	1.3577
Zehner, Bauer, Schlünder	1	Baule	Eq. (2)	$d_{dist} * \frac{\pi}{6}$	0.3360
	2	Baule	Eq. (6)	$d_{dist} * \frac{\pi}{6}$	0.3398
	3	Baule	Eq. (2)	$d_{peak} * \frac{\pi}{6}$	0.3432
Sphere model 2	1	Song	Eq. (6)	D_{prim} + KC	0.1185
primary particles	2	Song	Eq. (2)	D_{prim} + KC	0.1186
	3	Bauer	Eq. (2)	D_{prim} + KC	0.1204
Sphere model 2 aggregates					
Sphere model 2 agglomerate					
Zehner, Schlünder	1	Baule	Eq. (2)	$d_{peak} * \frac{\pi}{6}$	0.7804
primary particles	2	Baule	Eq. (6)	$d_{peak} * \frac{\pi}{6}$	0.7805
	3	Baule	Eq. (2)	$d_{dist} * \frac{\pi}{6}$	0.7807
Zehner, Schlünder aggregates					
Zehner, Schlünder agglomerate					
Slavin	1	Baule		d_{peak}	1.5975
primary particles	2	Baule		d_{dist}	1.5975
	3	Baule		$d_{peak} * \frac{\pi}{6}$	1.5975
Slavin aggregates					
Slavin agglomerate					

Supplementary material

Supplementary material associated with this article can be found, in the online version, at doi:10.1016/j.ijheatmasstransfer.2022.122519

References

[1] M. Alam, H. Singh, M.C. Limbachiya, Vacuum insulation panels (VIPs) for building construction industry – a review of the contemporary developments and future directions, Appl Energy 88 (11) (2011) 3592–3602, doi:10.1016/j.apenergy.2011.04.040.

[2] J. Fricke, U. Heinemann, H.P. Ebert, Vacuum insulation panels - from research to market, Vacuum 82 (7) (2008) 680–690, doi:10.1016/j.vacuum.2007.10.014.

[3] S.E. Wood, A mechanistic model for the thermal conductivity of planetary regolith: 1. the effects of particle shape, composition, cohesion, and compression at depth, Icarus 352 (2020) 113964, doi:10.1016/j.icarus.2020.113964.

[4] E.S. Huetter, N.I. Koemle, G. Kargl, E. Kaufmann, Determination of the effective thermal conductivity of granular materials under varying pressure conditions, Journal of Geophysical Research: Planets 113 (E12) (2008), doi:10.1029/2008JE003085.

[5] J. Ross-Jones, M. Gaedtke, S. Sonnick, M. Rädle, H. Nirschl, M.J. Krause, Conjugate heat transfer through nano scale porous media to optimize vacuum insulation panels with lattice boltzmann methods, Computers & Mathematics with Applications (2018), doi:10.1016/j.camwa.2018.09.023.

[6] J. Ross-Jones, M. Gaedtke, S. Sonnick, M. Meier, M. Rädle, H. Nirschl, M.J. Krause, Pore-scale conjugate heat transfer simulations using lattice boltz-

mann methods for industrial applications, Appl Therm Eng 182 (2021) 116073, doi:10.1016/j.applthermaleng.2020.116073.

[7] M. Wang, J. Wang, N. Pan, S. Chen, Mesoscopic predictions of the effective thermal conductivity for microscale random porous media, Physical Review E 75 (3) (2007) 036702, doi:10.1103/PhysRevE.75.036702. Publisher: American Physical Society

[8] S.-L. Wang, Z. Jin, J.-N. Li, B.-X. Zhang, Y.-B. Wang, Y.-R. Yang, X.-D. Wang, D.-J. Lee, Theoretical modeling of thermal conductivity of alumina aerogel composites based on real microstructures, J. Taiwan Inst. Chem. Eng. 120 (2021) 150–160, doi:10.1016/j.jtice.2021.03.003.

[9] B. Yu, P. Cheng, Fractal models for the effective thermal conductivity of bidispersed porous media, J. Thermophys Heat Transfer 16 (1) (2002) 22–29, doi:10.2514/2.6669. Publisher: American Institute of Aeronautics and Astronautics

[10] A.P. Senthil Kumar, V. Prabhu Raja, P. Karthikeyan, Comparison of geometry dependent resistance models with conventional models for estimation of effective thermal conductivity of two-phase materials, Heat Mass Transfer 46 (11) (2010) 1379–1394, doi:10.1007/s00231-010-0660-0.

[11] E. Tsotsas, H. Martin, Thermal conductivity of packed beds: a review, Chem. Eng. Process. 22 (1) (1987) 19–37, doi:10.1016/0255-2701(87)80025-9.

[12] S. Parzinger, Analytische Modellierung der temperatur- und gasdruckabhängigen effektiven Wärmeleitfähigkeit von Pulvern, Technical University Munich, 2014 Ph.D. thesis.

[13] H.T. Aichlmayr, F.A. Kulacki, The Effective Thermal Conductivity of Saturated Porous Media, in: G.A. Greene, J.P. Hartnett†, A. Bar-Cohen, Y.I. Cho (Eds.), Advances in Heat Transfer, volume 39, Elsevier, 2006, pp. 377–460, doi:10.1016/S0065-2717(06)39004-1.

[14] H. Bjurström, E. Karawacki, B. Carlsson, Thermal conductivity of a microporous particulate medium: moist silica gel, Int J Heat Mass Transf 27 (11) (1984) 2025–2036, doi:10.1016/0017-9310(84)90189-3.

[15] A.V. Luikov, A.G. Shashkov, L.L. Vasiliev, Y.E. Fraiman, Thermal conductivity of porous systems, Int J Heat Mass Transf 11 (2) (1968) 117–140, doi:10.1016/0017-9310(68)90144-0.

[16] S. Jayachandran, K.S. Reddy, Estimation of effective thermal conductivity of packed beds incorporating effects of primary and secondary parameters, Thermal Science and Engineering Progress 11 (2019) 392–408, doi:10.1016/j.tsep.2018.12.011.

[17] M. Bouquerel, T. Duforestel, D. Baillis, G. Rusaouen, Heat transfer modeling in vacuum insulation panels containing nanoporous silicas - a review, Energy Build 54 (2012) 320–336, doi:10.1016/j.enbuild.2012.07.034.

[18] C. Huang, G. Wei, L. Cui, Z. Zhou, X. Du, Gaseous thermal conductivity studies on mesoporous silica particles based on a bimodal-pore distribution model, Int. J. Therm. Sci. 160 (2021) 106668, doi:10.1016/j.ijthermalsci.2020.106668.

[19] M. Meier, S. Sonnick, E. Asylbekov, M. Rädle, H. Nirschl, Multi-scale characterization of precipitated silica, Powder Technol 354 (2019) 45–51, doi:10.1016/j.powtec.2019.05.072.

[20] M. Meier, Über den Entstehungsprozess poröser Strukturen am Beispiel der Partikelbildung von kolloidalem Silika und der Haufwerksbildung von gefällter Kieselsäure, Karlsruhe Institute of Technology, 2021 Ph.D. thesis.

[21] S. Pramanik, A. Manna, A. Tripathy, K.K. Kar, Current Advancements in Ceramic Matrix Composites, in: K.K. Kar (Ed.), Composite Materials, Springer Berlin Heidelberg, Berlin, Heidelberg, 2017, pp. 457–496, doi:10.1007/978-3-662-49514-8_14.

[22] E.H. Ratcliffe, Thermal conductivities of fused and crystalline quartz, Br. J. Appl. Phys. 10 (1) (1959) 22–25, doi:10.1088/0508-3443/10/1/306.

[23] Sovitec, Sovitec_msds_en_omicron_p0, 2016, https://www.sovitec.com/sites/default/files/2016-05/Sovitec_MSDS_En_Omicron_P0.pdf.

[24] S. Sonnick, M. Meier, J Ross-Jones, L. Erlbeck, I. Medina, H. Nirschl, M. Rädle, Correlation of pore size distribution with thermal conductivity of precipitated silica and experimental determination of the coupling effect, Appl Therm Eng (2019), doi:10.1016/j.applthermaleng.2019.01.074.

[25] P.A. Chambre, S.A. Schaaf, Flow of rarefied gases, Princeton University Press, 2017.

[26] E.H. Kennard, Kinetic theory of gases, volume 483, McGraw-hill New York, 1938.

[27] P.W. Atkins, J.d. Paula, Wärmeleitung, in: Physikalische Chemie, John Wiley & Sons, 2006, pp. 672–673.

[28] R.S. Prasolov, Generalization of the equation of the thermal conductivity of gases, Izv. VUZ'ov, Priborostr. (1961).

[29] M.G. Kaganer, Thermal insulation in cryogenic engineering, Israel Program for Scientific Translations, 1969. http://cds.cern.ch/record/103864

[30] S.Q. Zeng, A. Hunt, R. Greif, Mean free path and apparent thermal conductivity of a gas in a porous medium, J Heat Transfer 117 (3) (1995) 758–761, doi:10.1115/1.2822642.

[31] J. Fricke, X. Lu, P. Wang, D. Büttner, U. Heinemann, Optimization of monolithic silica aerogel insulants, Int J Heat Mass Transf 35 (9) (1992) 2305–2309, doi:10.1016/0017-9310(92)90073-2.

[32] O. Krischer, Die Grundlagen der Wärmeübertragung, in: O. Krischer, W. Kast (Eds.), Trocknungstechnik: Die wissenschaftlichen Grundlagen der Trocknungstechnik, Springer, Berlin, Heidelberg, 1978, pp. 68–168, doi:10.1007/978-3-642-61879-6_5.

[33] N. Wakao, S. Kagei, Heat and mass transfer in packed beds, Taylor & Francis, 1982.

[34] P. Zehner, E.U. Schlünder, Einfluß der wärmestrahlung und des druckes auf den wärmetransport in nicht durchströmten schüttungen, Chem. Ing. Tech. 44 (23) (1972) 1303–1308, doi:10.1002/cite.330442305.

[35] K. Denpoh, Modeling of rarefied gas heat conduction between wafer and susceptor, IEEE Trans. Semicond. Manuf. 11 (1) (1998) 25–29, doi:10.1109/66.661281.

[36] K. Swimm, S. Vidi, G. Reichenauer, H.P. Ebert, Coupling of gaseous and solid thermal conduction in porous solids, J Non Cryst Solids 456 (2017) 114–124, doi:10.1016/j.jnoncrysol.2016.11.012.

[37] J.F. Guo, G.H. Tang, A theoretical model for gas-contributed thermal conductivity in nanoporous aerogels, Int J Heat Mass Transf 137 (2019) 64–73, doi:10.1016/j.ijheatmasstransfer.2019.03.106.

[38] B. Baule, Theoretische behandlung der erscheinungen in verdünnten gasen, Ann Phys 349 (9) (1914) 145–176, doi:10.1002/andp.19143490908.

[39] F.O. Goodman, H.Y. Wachman, Formula for thermal accommodation coefficients, J. Chem. Phys. 46 (1967) 12.

[40] S. Song, M.M. Yovanovich, Correlation of thermal accommodation coefficient for 'engineering' surfaces, ASME HTD 69 (1987) 107–116. http://www.mhtl.uwaterloo.ca/old/paperlib/papers/contact/gap_cond/engineer.pdf

[41] R. Bauer, Effektive radiale wärmeleitfähigkeit gasdurchströmter schüttungen mit partikeln unterschiedlicher form und größenverteilung: Mit 7 tafeln, VDI-Verl., Düsseldorf, 1977.

[42] G.M. Kremer, Basic Principles of the Kinetic Theory, in: G.M. Kremer (Ed.), An Introduction to the Boltzmann Equation and Transport Processes in Gases, Springer, Berlin, Heidelberg, 2010, pp. 1–35, doi:10.1007/978-3-642-11696-4_1.

[43] C.W. Kosten, The mean free path in room acoustics, Acta Acustica united with Acustica 10 (4) (1960) 245–250.

[44] S.V. Belov, O.G. Kartuesov, V.M. Polyaev, Mean pore size of porous metals, Soviet Powder Metallurgy and Metal Ceramics 11 (9) (1972) 733–734, doi:10.1007/BF00801273.

[45] S. Sonnick, M. Meier, G. Ünsal Peter, L. Erlbeck, H. Nirschl, M. Rädle, Thermal accommodation in nanoporous silica for vacuum insulation panels, International Journal of Thermofluids 1–2 (2020) 100012, doi:10.1016/j.ijft.2019.100012.

[46] X. Lu, R. Caps, J. Fricke, C.T. Alviso, R.W. Pekala, Correlation between structure and thermal conductivity of organic aerogels, J Non Cryst Solids 188 (3) (1995) 226–234, doi:10.1016/0022-3093(95)00191-3.

[47] Z. Kovács, S. Szanyi, I. Budai, K. Lakatos, Laboratory Tests of High-Performance Thermal Insulations, in: J. Littlewood, R.J. Howlett, A. Capozzoli, L.C. Jain (Eds.), Sustainability in Energy and Buildings, Springer Singapore, Singapore, 2020, pp. 73–82.

[48] H.W. Russell, Principles of heat flow in porous insulators, J. Am. Ceram. Soc. 18 (1) (1935) 1–5, doi:10.1111/j.1151-2916.1935.tb19340.x.

[49] J.C. Maxwell, A treatise on electricity and magnetism, volume 1, Oxford: Clarendon Press, 1873.

[50] G.R. Cunnington, C.L. Tien, Heat Transfer in Microsphere Insulation in the Presence of a Gas, in: V.V. Mirkovich (Ed.), Thermal Conductivity 15, Springer US, Boston, MA, 1978, pp. 325–333, doi:10.1007/978-1-4615-9083-5_39.

[51] K.H. Brodt, Thermal insulations Cfc - alternatives and vacuum insulation, Technische Universiteit Delft, 1995 Ph.D. thesis. https://repository.tudelft.nl/islandora/object/uuid%3A2bc13442-c6c0-4ded-8948-3e65518ab305

[52] R.G. Deissler, C.S. Eian, Investigation of effective thermal conductivities of powders, National Advisory Committee for Aeronautics (1952).

[53] D. Kunii, J.M. Smith, Heat transfer characteristics of porous rocks: II. thermal conductivities of unconsolidated particles with flowing fluids, AIChE J. 7 (1) (1961) 29–34, doi:10.1002/aic.690070109.

[54] M. Matsushita, M. Monde, Y. Mitsutake, Predictive calculation of the effective thermal conductivity in a metal hydride packed bed, Int J Hydrogen Energy 39 (18) (2014) 9718–9725, doi:10.1016/j.ijhydene.2014.04.072.

[55] T. Schumann, V. Voss, Heat flow through granulated material, Fuel 13 (8) (1934) 249–256.

[56] P. Zehner, E.U. Schlünder, Wärmeleitfähigkeit von schüttungen bei mäßigen temperaturen, Chem. Ing. Tech. 42 (14) (1970) 933–941, doi:10.1002/cite.330421408.

[57] S.S. Sih, J.W. Barow, The prediction of the emissivity and thermal conductivity of powder beds, Part. Sci. Technol. 22 (4) (2004) 427–440, doi:10.1080/02726350490501682. Publisher: Taylor & Francis

[58] K. Swimm, G. Reichenauer, S. Vidi, H.-P. Ebert, Gas pressure dependence of the heat transport in porous solids with pores smaller than 10 microns, Int J Thermophys 30 (4) (2009) 1329–1342, doi:10.1007/s10765-009-0617-z.

[59] A.J. Slavin, V. Arcas, C.A. Greenhalgh, E.R. Irvine, D.B. Marshall, Theoretical model for the thermal conductivity of a packed bed of solid spheroids in the presence of a static gas, with no adjustable parameters except at low pressure and temperature, Int J Heat Mass Transf 45 (20) (2002) 4151–4161, doi:10.1016/S0017-9310(02)00117-5.

[60] T. Feng, A. Rai, D. Hun, S.S. Shrestha, Molecular dynamics simulations of energy accommodation between gases and polymers for ultra-low thermal conductivity insulation, Int J Heat Mass Transf 164 (2021) 120459, doi:10.1016/j.ijheatmasstransfer.2020.120459.

[61] A.T. Rosenberger, E.B. Dale, D. Ganta, J.P. Rezac, Investigating properties of surfaces and thin films using microsphere whispering-gallery modes, in: Laser Resonators and Beam Control X, volume 6872, International Society for Optics and Photonics, 2008, p. 68720U, doi:10.1117/12.772655.